Experimentally validated meso-scale fracture modelling of foamed concrete

Jiang, Nengdong; Ge, Zhi; Guan, Yanhua ; Zuo, Zhiwu ; Zhang, Hongzhi; Ling, Yifeng ; Šavija, Branko

DOI
10.1016/j.tafmec.2022.103631

Publication date
2022

Document Version
Final published version

Published in
Theoretical and Applied Fracture Mechanics

Theoretical and Applied Fracture Mechanics 122 (2022) 103631

Contents lists available at ScienceDirect

Theoretical and Applied Fracture Mechanics

journal homepage: www.elsevier.com/locate/tafmec

Experimentally validated meso-scale fracture modelling of foamed concrete

Nengdong Jiang [a], Zhi Ge [a], Yanhua Guan [a], Zhiwu Zuo [b], Hongzhi Zhang [a,c,*], Yifeng Ling [a,*], Branko Šavija [d]

[a] School of Qilu Transportation, Shandong University, 250002 Jinan, PR China
[b] Shandong Hi-speed Group, 250098 Jian, PR China
[c] Suzhou Research Institute, Shandong University, Suzhou 215021, PR China
[d] Microlab, Faculty of Civil Engineering and Geosciences, Delft University of Technology, 2628 CN Delft, the Netherlands

ARTICLE INFO

Keywords:
Foamed concrete
Mechanical properties
Discrete lattice model
Air-void structure

ABSTRACT

This work presents a study of mechanical properties of foamed concrete at the meso-scale based on a combination of X-ray computed tomography (XCT) technique and a discrete lattice type fracture model. The microstructure of the foamed concrete with different densities was obtained by XCT technique and binarized as two-phase (pore/solid) materials. The parameters (e.g., porosity, pore diameter and spacing distribution) of foamed concrete air-void structure were characterized. The virtual specimens were subjected to computational uniaxial compression, Brazilian splitting and three-point bending test to calculate strengths and elastic modulus. The mechanical properties of solid phase were derived from the recent outcome of micromechanical models. Two types of element input parameters were used to investigate the influence of the input parameters on the simulated results. The modelling results (strength value and fracture pattern) were compared with the experiments. It shows that, without further calibration, the lattice model can predict the mechanical strength and crack pattern with good accuracy. The fracture toughness K_{IC} was derived using three-point bending strength and the average pore diameter. The results indicate that the presence of air-void structure increases the brittleness and reduces the fracture toughness of the foamed concrete.

1. Introduction

Foamed concrete is a light cellular construction material with random air voids created by the entrapped foam agent [1]. It can be designed to have a density ranging between 400 kg/m^3 and 1900 kg/m^3 [2–4]. Due to its interesting characteristics such as self-compacting, low unit weight, adjustable compressive strength and convenient preparation, it has been widely applied in structural members [5–7], filling grades [8–10], and road embankment infills [11].

Due to the wide application of foamed concrete in the field of engineering, understanding of its mechanical properties and fracture behavior is of great interest. The mechanical properties of foamed concrete are affected by a number of parameters, such as density, binder material, water/binder ratio, curing condition and air-void structure [12,13]. It has been reported that compressive strength has a direct relationship with density where a reduction in density adversely affects the strength [3]. The pore size in foamed concrete can vary from nanometer to millimeter, and is one of the major factors affecting its mechanical properties [14–19]. Guo et al [20]and Nguyen et al [21] have correlated the mechanical properties of foamed concrete with pore parameters, such as shape factor (flatness index and elongation index) and sphericity. Nambiar et al. [22] observed that higher porosity seems to produce larger voids, resulted in wide distribution of void sizes and lower strength. Kuzielová et al. [23] proposed that a decrease in pore size promoted the increase of the strength of foamed concrete.

In addition to the experiments, numerous efforts have been made to model the fracture behavior of foamed concrete. In terms of the fracture model, two aspects should be considered. The first one is how to obtain a realistic material structure, especially the pore structure. This can be achieved by numerical approaches or experiments. Compared with experiments, the computer generated material structure models [24] are easier and faster. However, pores are generally described as spheres in this approach, which is not always correct for foamed concrete. Therefore, although the experimentally obtained material structure has a disadvantage in terms of spatial resolution, the realistic pore shape and size distribution can be captured. Over the past decades, huge advances

* Corresponding authors at: School of Qilu Transportation, Shandong University, 250002 Jinan, PR China.
E-mail addresses: hzzhang@sdu.edu.cn (H. Zhang), yfling@sdu.edu.cn (Y. Ling).

https://doi.org/10.1016/j.tafmec.2022.103631
Received 28 March 2022; Received in revised form 7 October 2022; Accepted 10 October 2022
Available online 17 October 2022

Table 1
Chemical compositions of the P.I 42.5 cement.

Materials	SiO_2	Al_2O_3	Fe_2O_3	CaO	MgO	SO_3	Na_2O	LOI
OPC	20.08	5.09	3.81	63.41	2.06	2.33	0.55	1.72

Table 2
Mixing proportion of prepared foamed concrete.

Mix	Targeted wet density (kg/m^3)	w/c	Cement (kg/m^3)	Water (kg/m^3)	Foam (kg/m^3)
M600	600	0.5	386	193	20.5
M700	700	0.5	454	227	18.8
M800	800	0.5	521	261	17.2

Table 3
Mechanical tests performed on foamed concrete.

Mechanical properties	Sample dimension (mm)	Loading speed
Uniaxial compression strength	40 mm × 40 mm × 40 mm	0.8 mm/min
Brazilian splitting strength	40 mm × 40 mm × 40 mm	1 mm/min
Three-point bending strength	40 mm × 40 mm × 160 mm	0.2 mm/min
Elastic modulus	100 mm × 100 mm × 300 mm	–

have been made in the microstructural characterization techniques. A good resolution of the microstructure can be provided by scanning electron microscopy (SEM) [25]. Ge et al.[4] observed the pore structure of foamed concrete using SEM and calculated the pore size distribution. However, the main shortcoming of this technique is that only 2D microstructural information can be captured. X-ray Computed Tomography (XCT) is a nondestructive technique for visualizing interior features within solid objects. It can be used to resolve full 3D microstructure of cementitious materials with spatial information on pore and solid phase, thus becoming an attractive technique for acquiring a 3D microstructure of foamed concrete [26,27]. In Ref [28], foamed concrete is described as porous matrix-inclusion material by means of X-ray tomography. She et al. [29] used XCT to study the hydration products and the microstructure of foamed concrete.

The second aspect is applying a suitable mechanical model to simulate the mechanical properties and fracture behavior of the generated material structure. At the mesoscale, both continuum-based and discrete-based numerical approaches have been utilized. These include lattice model [30,31], discrete element model (DEM) [32–34] and continuum model [35,36] etc. In lattice model, the continuum is depicted by a collection of discrete beam elements. The heterogeneity of materials at meso-scale is performed by assigning different mechanical properties of these beams. The fracture is accounted with the beam stiffness deterioration and eventual removal [30,31,37]. As for DEM, the materials constituents were modeled by discal, spherical [34] and polygonal particles [38]. The force transfer between particles is achieved through contact interaction. The motion of the particles is resolved using rigid body dynamics [39]. Inter-particle spring elements are inserted to model the cohesion between the various phases of the materials. The spring elements enable separation of the particles when the internal force of spring exceeds the bond strength [40]. In this way, the fracture process can be simulated. The continuum models are generally based on the finite element method (FEM) [41,42] and some investigations were carried out based on peridynamics [43]. In these models, the fracture process are explicitly simulated using interface elements [44,45], damage models [46,47] or the extended FEM [48]. Several models have been utilized to investigate the mechanical properties of foamed concrete. For example, Viejo et al. [49] utilized concrete damage plasticity (CDP) model to estimate and predict the compressive and tensile strengths of porous cementitious materials. Ref. [50] used the CDP model in ABAQUS to model the compressive behavior of foamed concrete and elucidated the failure mechanism of foamed concrete. Kim et al [51] investigated the mechanical responses of foamed concrete under uniaxial tension using the phase-field fracture model and correlated the mechanical responses with microstructural characteristics. In Ref. [52], the DEM was calibrated and validated based experimental results and was used to characterize the compressive behavior of foamed concrete. However, it is worth mentioning that the physical dimension of the specimen simulated by the numerical models are quite different from the tested specimen. The simulated mechanical properties are therefore questionable on guiding the experimental design because of the size effect [53–55].

To this end, a comparison between experiments and numerical modelling was carefully designed in the current study. The physical dimension of tested and simulated specimens is kept the same. Foamed concretes with various wet densities (600 kg/m^3, 700 kg/m^3 and 800 kg/m^3) and multiple loading conditions (uniaxial compression, Brazilian splitting and three-point bending) were considered. The foamed

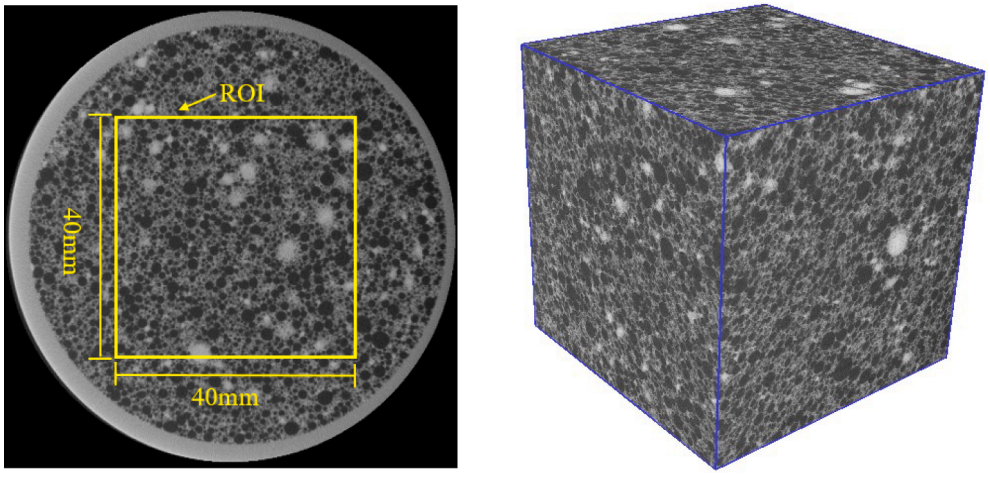

Fig. 1. Schematic diagram of ROI: (a) An example cross sectional XCT image of ROI; (b) 3D diagram of ROI.

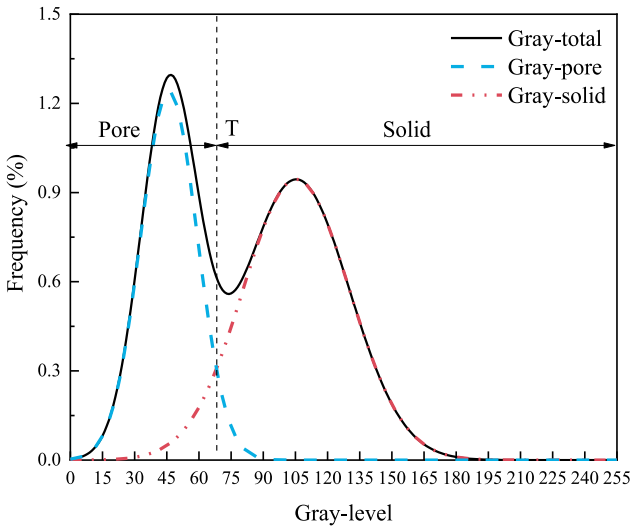

Fig. 2. Phases evolution through greyscale level histogram of CT images.

concrete was modelled as a two-phase material. Its material structure was derived from XCT scanning. A discrete lattice model was used for modelling the fracture process and predicting the mechanical properties (e.g. strength and elastic modulus). As a compromise between computational efficiency and model accuracy, a two-dimensional model was adopted herein. As it has been shown in the literature that the introduced air voids has limited effect on the properties of the binder material [56], constitutive relations of the hydrated cement paste were directly derived from the results of micromechanical model presented in the authors' previous work [57]. In order to consider the stochastic features of pore structure, ten 2D material structures were randomly selected from the XCT images. The reasonable agreement between simulation and experiment shows that the proposed modelling strategy is capable for prediction of mechanical properties and fracture behavior of foamed concrete. The fracture toughness K_{IC} was determined through three-point bending strength and the average pore diameter. In addition, the

Table 4
Porosity of foamed concrete for each mix.

Mix	Porosity (%)
M600	37.72 %
M700	30.59 %
M800	24.38 %

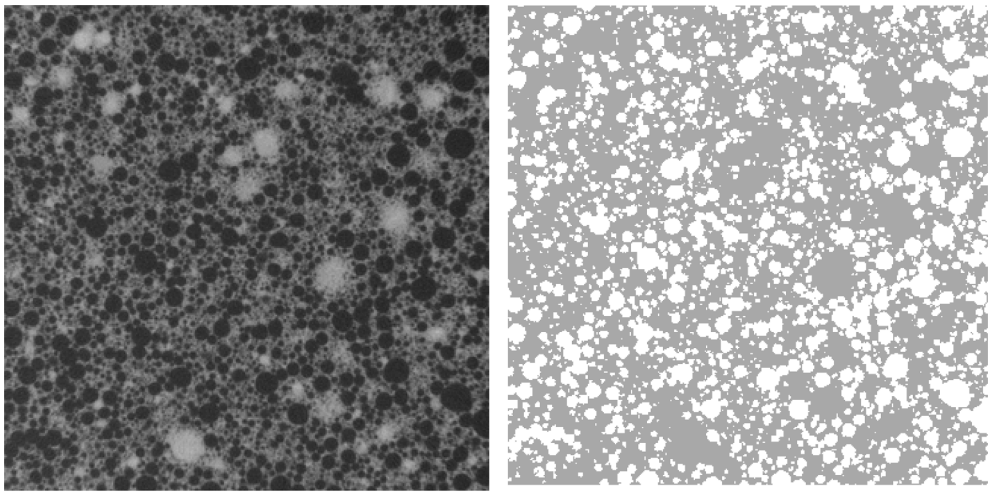

(a) **(b)**

Fig. 3. Comparison of the image before and after image segmentation. (a) original grayscale image;(b) pore (white)and solid phases (grey) are isolated from the greyscale map.

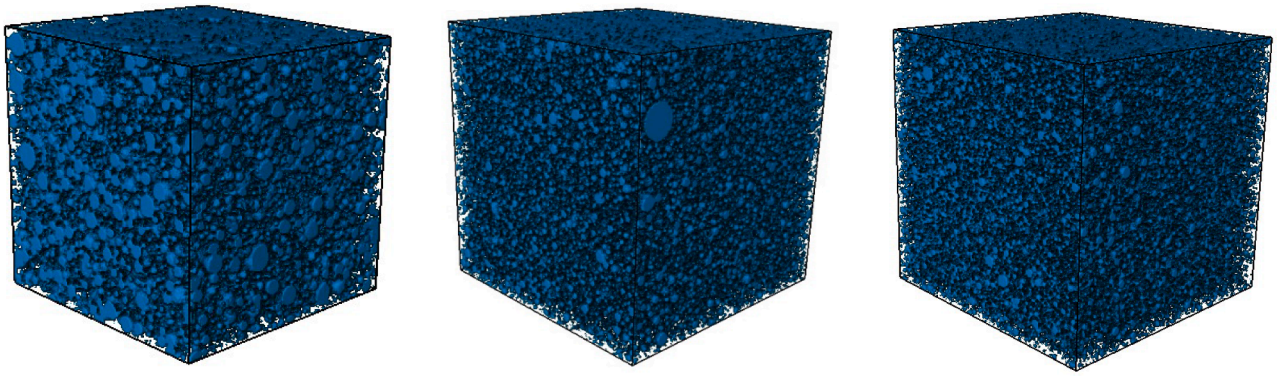

(a) (b) (c)

Fig. 4. The spatial distribution of the segmented pore phase for each mix: (a) M600 ; (b) M700 ; (c) M800.

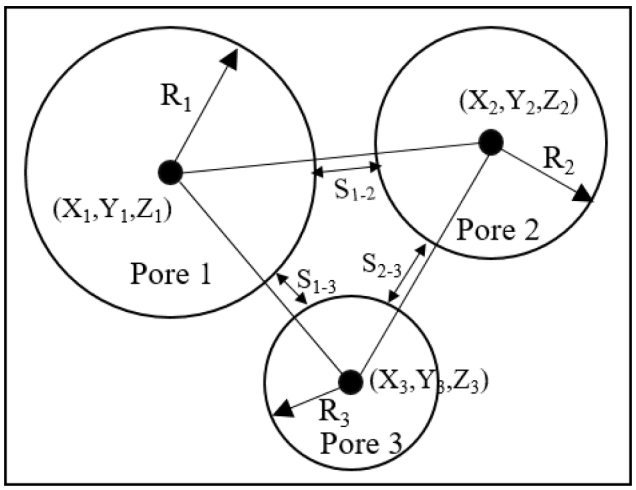

Fig. 5. The schematic diagram of air-voids spacing.

effects of porosity on mechanical properties for foamed concrete were examined a widely used empirical equation.

2. Experimental

2.1. Materials and sample preparation

P.I 42.5 Portland cement produced by Fushun Cement Incorporated Company (Liaoning, China), a protein-based anionic foaming agent ordered from Chilong Building Energy Saving Technology Co. ltd (Shandong, China) and water were used to prepare the foamed concrete in this study. Chemical composition of the cement used, as provided by the supplier, are shown in.

Table 1. The foaming agent has a dilution ratio of about 40–50 and the foaming ratio is about 1000–1200.

Mixtures with wet density of 600 kg/m^3, 700 kg/m^3 and 800 kg/m^3 were designed. The water to binder ratio was 0.5 for all the mixtures. The proportions are shown in Table 2. A pre-foaming method [3] was used for the mixture preparation. Water was first mixed with the cement at a low speed of 145 ± 5 rm for 90 s. This was followed by a 60 s high speed (285 ± 10 rm) mixing process. Simultaneously, standard foam with density of 40 kg/m^3 was produced and doped into the paste to mix evenly until there was no white foam floating on the surface of the mixture. Before casting, the wet density was measured. Then, the fresh mixture was poured into molds and covered with plastic sheet to prevent water evaporation. After 24 h, the samples were demolded and stored in a curing room (≥95 % relative humidity (RH), 20 ± 2 ℃) for 28 days.

2.2. Mechanical loading

For the mechanical properties test, specimens with dimensions described in Table 3 were cast and used for uniaxial compression, Brazilian splitting, three-point bending and elastic modulus measurements. Considering the heterogeneity of foamed concrete and its effect on deformation and fracture properties, 10 specimens were used for each of the tests. Crucial parameters for these mechanical tests are listed in Table 3.

2.3. X-ray computed tomography and image processing

Cylindrical sample (Φ75mm × 200 mm) was prepared for each mix and fixed in the rotatable stage of a high resolution micro-XCT system (ZEISS Xradia 510 Versa) for acquiring raw greyscale images with a source voltage of 140 kv and current of 72 mA. The sample was rotated from 0° to 360°. 2000 shadow projections with a pixel size of 100 μm were acquired (1004 × 1024 pixels). Each projection image was averaged with an exposure time of 1.2 s. The reconstruction work was conducted by the Dragonfly software. To reduce the influence of beam hardening in the XCT experiment, a cubic region of interest (ROI) with length of 40 mm was extracted from center of the specimen for threshold determination which was used to segment pore and solid phase, see Fig. 1. From Fig. 1, it is possible to observe features of pore (black), hydration product (grey), and unhydrated cement grains (white). In case of simplification, the foamed concrete was simplified as a two-phase (pore and hydrated cement paste, i.e., solid phase) material. A deconvolution approach was adopted to fit the greyscale level histogram by two Gaussian distributions [51,58–60], see Fig. 2. The threshold grey value (T) between pore and solid phases was therefore defined as the

Table 5
Average pore diameter and pore spacing of foamed concrete.

Mix	Average pore diameter (μm)	Average pore spacing (μm)
M600	744.33	120.56
M700	419.47	105.52
M800	371.55	105.60

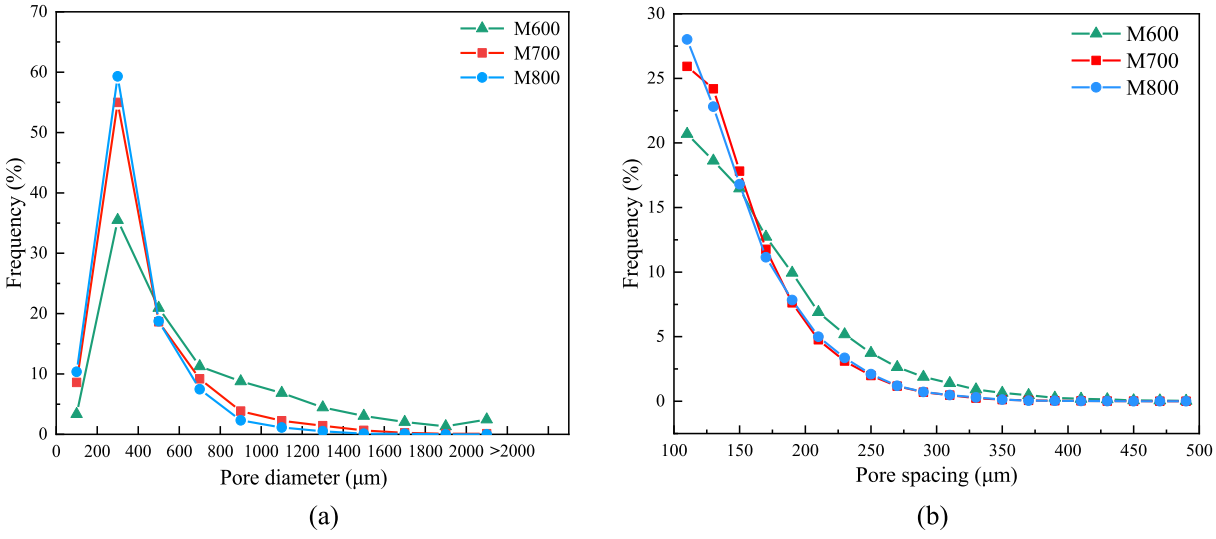

Fig. 6. (a) Pore diameter distribution; (b) Pore spacing distribution.

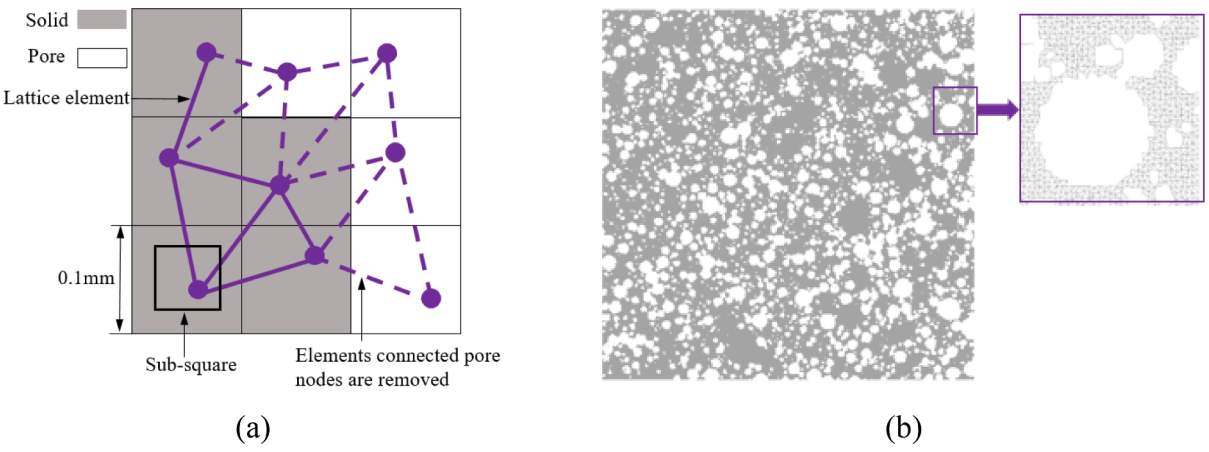

Fig. 7. (a) overlay procedure for a 2D lattice mesh; (b) 2D Lattice model of foamed concrete based XCT image.

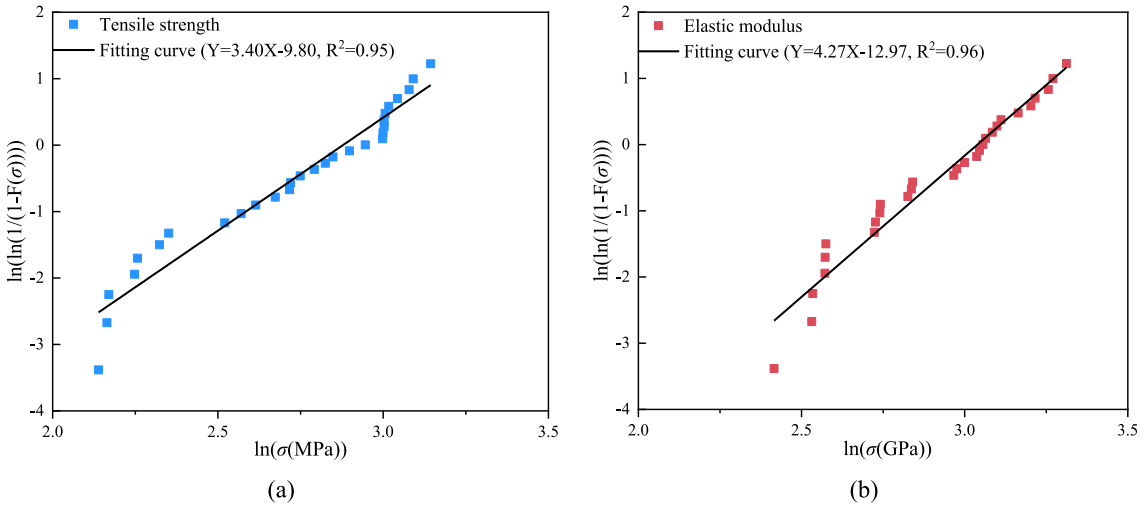

Fig. 8. Weibull plot of input parameters: (a) Tensile strength, (b) Elastic modulus.

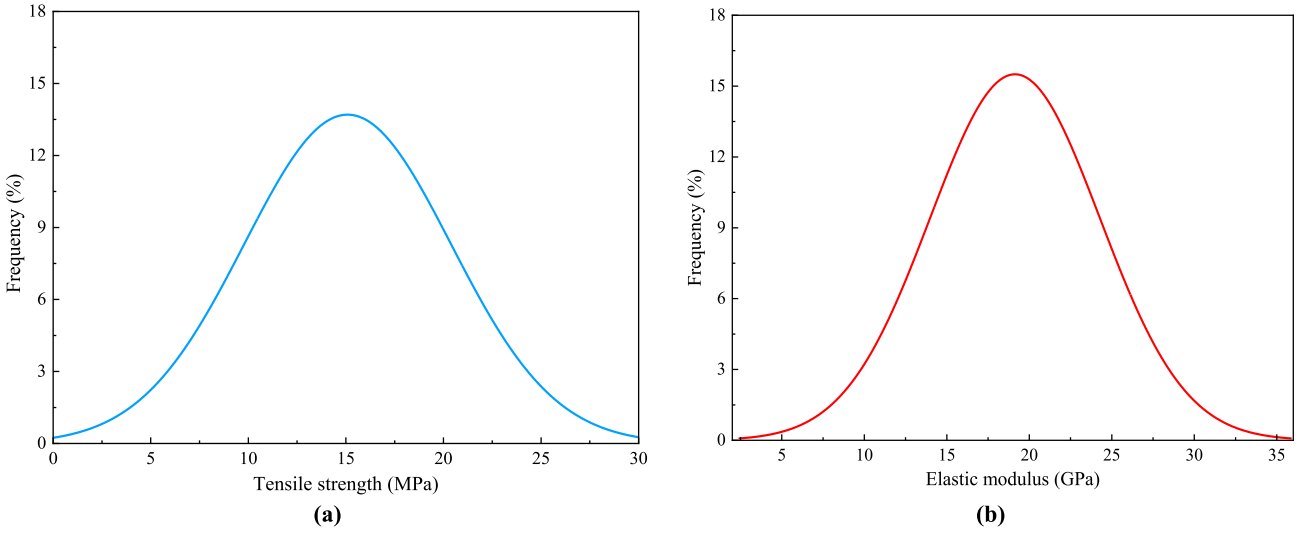

Fig. 9. Weibull distribution curves of tensile strength and elastic modulus of lattice elements:(a) Tensile strength, (b) Elastic modulus.

intersection of the two Gaussian curves. Fig. 3 compares the image before and after image segmentation. Fig. 4 shows the spatial distribution of the segmented pore phase for each mix. The porosity can be calculated by the volume ratio between the pore phase and ROI. Note that pores smaller than 100 μm cannot be detected due to the limits of CT image resolution.

Table 6
Input parameters of the lattice model.

Model	Elastic modulus (GPa)		Tensile strength (MPa)	
Model-I	Weibull distribution			
	m	*η*	*m*	*η*
	4.27	20.85	3.40	17.86
Model-II	Average			
	19.36		16.25	

The calculated porosity of each mixture is shown in Table 4. They are consistent with the porosity derived using similar strategies [51,61]. As expected, the porosity increases with the decrease of targeted wet density.

2.4. Pore structure analysis

It is well-known that the size and spatial distribution of pore have a significant influence on the mechanical performance of the porous materials. They can be determined based on the segmented pore phase from ROI. Calculation of pore size distribution was performed using a procedure presented by Dong et al. [62,63]. The pore spacing was defined as the minimum distance among pores. As shown in Fig. 5, $S_{1\text{-}3}$ is smaller than $S_{2\text{-}3}$, and used to define the spacing of Pore 3. The distance between pores can be calculated using the following Eq (1).

$$S_{1,2} = \sqrt{(X_1 - X_2)^2 + (Y_1 - Y_2)^2 + (Z_1 - Z_2)^2} - R_1 - R_2 \quad (1)$$

Here, X, Y, and Z represent the coordinates of the center of the pore.

The 3D pore size distribution and pore spacing distribution are shown in Fig. 6. There are a few pores larger than 500 μm present and the amount of these pores increases with porosity, which may be caused by merging and overlapping of smaller pores [20,24,56,64]. The pore diameter is mainly concentrated in the range of 0.2 mm and 0.8 mm, which accounts for more than 50 % of the total pores for all mixes. The amount of pores decreases as the spacing gets larger. The spacing of most pores is smaller than 150 μm. The mean equivalent pore diameter and pore spacing are shown in Table 5. Clearly, the mean pore diameter decreases as the density increases. The average pore size and spacing of M600 is the largest among all mixes.

3. Modelling

3.1. Modelling approach

Discrete lattice fracture models have been widely used to simulate deformation and fracture of concrete[30,65,66]. The theory and concept behind the model can be found in [67,68]. In the lattice model, the continuum is schematized as a set of beam elements that can transfer axial and shear forces and bending moments. All individual elements are defined having linear elastic behavior. In order to consider the effect of shear deformation, Timoshenko beam elements with a low ratio of length to height was used [69,70]. Each element represents the properties of a small volume of material. The material heterogeneity can be easily considered by overlaying a material structure to the lattice mesh.

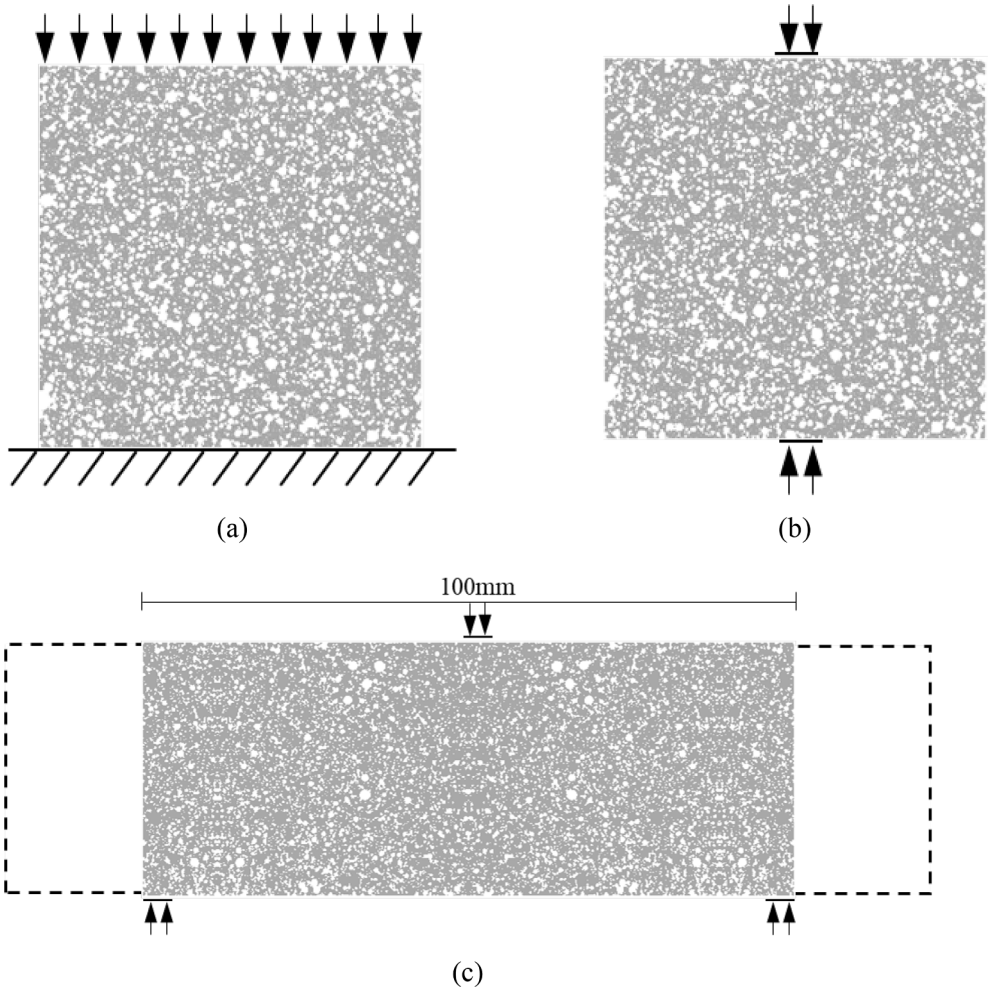

Fig. 10. Boundary conditions: (a) Uniaxial compression; (b) Brazilian splitting; (c) Three-point bending.

Table 7
Measured mechanical properties of foamed concrete.

Targeted wet density (kg/m^3)	Compressive strength (MPa)	Brazilian splitting strength (MPa)	Three-point bending strength (MPa)	Elastic modulus (GPa)
600	2.58	0.30	0.65	1.31 ± 0.07
	1.92	0.37	0.73	
	2.76	0.37	0.67	
	2.44	0.34	0.71	
	2.70	0.39	0.56	
	2.13	0.30	0.52	
	1.85	0.34	0.57	
	2.28	0.41	0.52	
	2.31	0.36	0.54	
	2.08	0.34	0.56	
Average	2.30 ± 0.32	0.35 ± 0.04	0.60 ± 0.08	
700	3.24	0.43	1.04	1.97 ± 0.06
	2.44	0.50	1.16	
	3.02	0.46	1.15	
	2.89	0.48	1.09	
	3.19	0.49	1.00	
	2.52	0.47	0.95	
	2.68	0.48	0.96	
	3.14	0.49	1.10	
	2.71	0.50	0.92	
	2.77	0.52	0.96	
Average	2.86 ± 0.28	0.48 ± 0.03	1.04 ± 0.09	
800	3.71	0.54	1.37	2.65 ± 0.11
	3.85	0.59	1.35	
	4.08	0.58	1.20	
	4.01	0.60	1.28	
	3.51	0.61	1.37	
	3.43	0.55	1.23	
	3.95	0.51	1.20	
	3.53	0.53	1.35	
	3.48	0.55	1.10	
	3.80	0.59	1.15	
Average	3.74 ± 0.24	0.57 ± 0.03	1.26 ± 0.10	

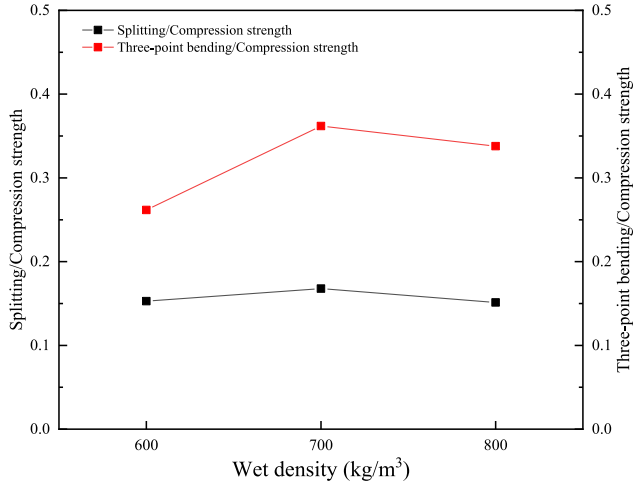

Fig. 11. α_{sc} (black) and α_{tc} (red) of three mixes. (For interpretation of the references to colour in this figure legend, the reader is referred to the web version of this article.)

To simulate the crack growth, a sequentially linear analysis approach is adopted. In this way, unit prescribed displacement is imposed on the lattice system, and a single element with the highest stress/strength ratio is removing from the mesh at every loading step. This element is then recorded as "failed" and removed from the mesh. The mesh is updated and relaxed, then the loading is redistributed. The calculation procedure will repeat until a predefined stopping criterion (e.g., load or displacement) is reached. This method can express the physical process of fracture behavior, so that a realistic crack patterns as well as the stress–strain response is obtained [71]. The procedure to generate the lattice mesh and assign mechanical properties of elements is as follows.

First, a square with length of 40 mm (400 pixels) was randomly extracted from the greyscale images obtained by XCT. Then a cell was defined within each pixel and the node was randomly placed in it, as shown Fig. 7a. The ratio between the size of cell and pixel defines the randomness of the mesh. The randomness not only affects the simulated fracture pattern [30], but also determines the Poisson's ratio of the mesh. In order to avoid large variations in length of element and introduce geometry disorder of material texture, a randomness of 0.5 is adopted. This randomness results in a Poisson's ratio of 0.18 for the global system, which is close to the cementitious materials. The final lattice network was generated through Delaunay triangulation, see Fig. 7b, as described by [68]. Two types of element were defined according to the location of two ends of the element, namely: cement paste and pore elements. The elements that have an end in the pore were removed from the model, which means that the strength is 0, as shown in Fig. 7a.

A series of linear elastic analysis was performed by calculating the stress in each beam element based on the specific external boundary condition. Normal force and bending moment were taken into account for the stress calculation:

$$\alpha = \alpha_N \frac{N}{A} + \alpha_M \frac{\max(M_X, M_Y)}{W} \tag{2}$$

where N is the normal force along the element. M_x and M_y are the bending moments in the local coordinate system. A is the beam cross-sectional area. W is the cross-sectional moment of resistance. The coefficients α_N and α_M denote the normal force factor and the bending moment influence factor. Their values are commonly adopted as 1.0 and 0.05, respectively [37]. Ref [72] discussed the influence of these parameter values on the concrete fracture response.

In the present research, a multi-scale simulation scheme developed by Zhang [53,73] was used to determine the input mechanical properties of cement paste. The input mechanical parameters of cement paste at the meso-scale were derived from results of micromechanical modelling. Note that the resolution at the meso-scale was chosen to match the size of the investigated size of material volume at the micro-scale. The readers are referred to Ref. [57,74,75] for more details about the micromechanical modelling and Ref.[53,73,76] for the up-scaling approach.

To consider the influence of the variation of input parameter on the simulated behavior, two modelling strategies were used. The first one (Model-I) assumed the input parameters follow a Weibull distribution (Eq.3).

$$F(\sigma) = 1 - \exp[-(\frac{\sigma}{\eta})^m] \tag{3}$$

where σ is the fracture strength or elastic modulus, η is the scaling parameter (characteristic strength), m is the shape parameter which is used to describe variability in measured material strength of brittle materials. These parameters were fitted from the results presented in the authors' previous study [57]. Fig. 8 shows the fitted results. The tensile strengths and elastic moduli derived from the micromechanical simulation are plotted in a Weibull coordinate system. A least-squares method was used adopted. The distribution of tensile strengths and elastic modulus are shown in Fig. 9. The second one adopted the input elastic modulus and strength of hydrated cement paste as constant and termed as Model-II. The constants were the average of the simulation results presented in Ref. [57]. Table 6 shows the two groups of input parameters.

3.2. Boundary conditions

The boundary conditions for the computational uniaxial

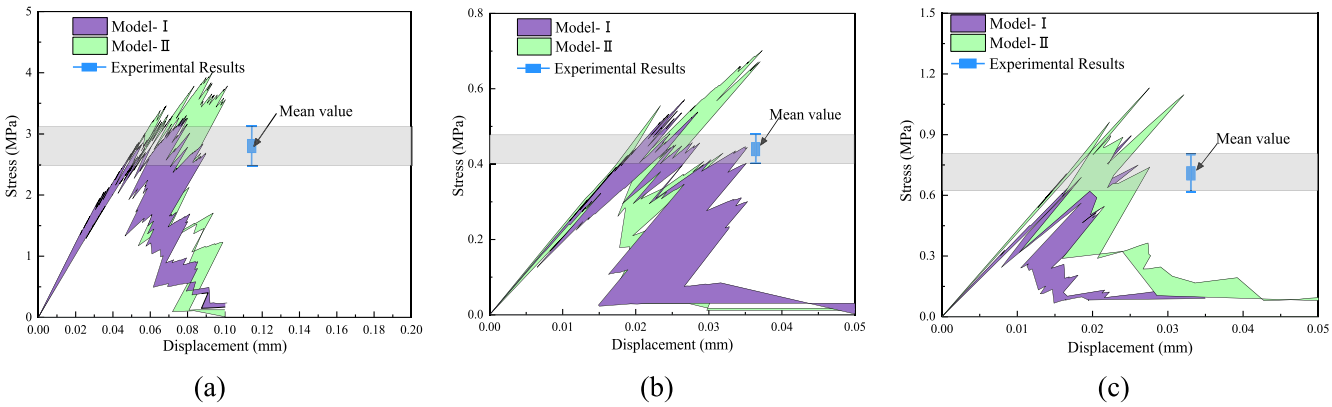

Fig. 12. The comparison between simulated and experimental results: (a) Uniaxial compression; (b) Splitting tension; (c) Three-point bending.

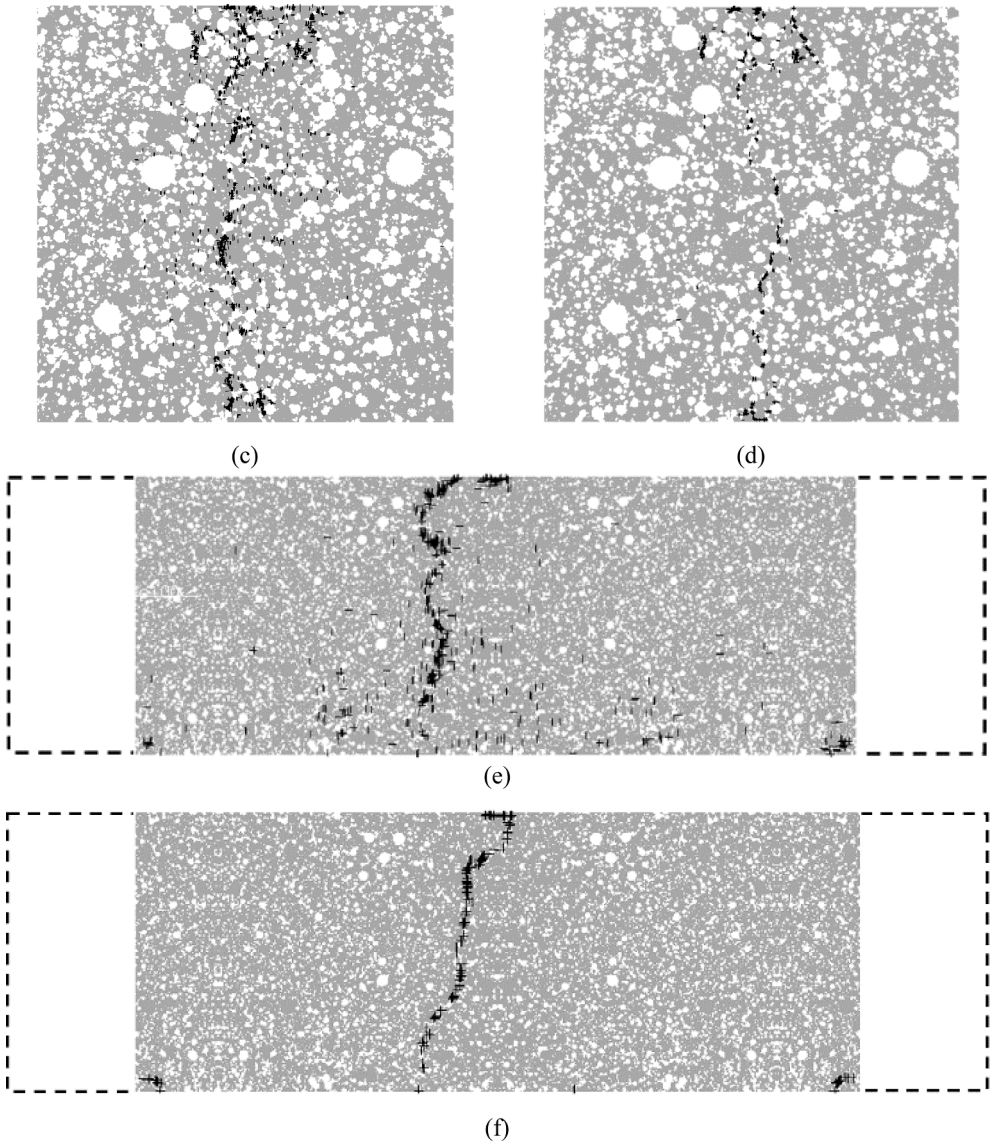

Fig. 13. Comparison of the simulated final fracture pattern of different mechanical properties: (a) Uniaxial compression with Model-I; (b) Uniaxial compression with Model-II; (c) Brazilian splitting with Model-I; (d) Brazilian splitting with Model-II; (e)Three-point bending with Model-I; (e)Three-point bending with Model-II.

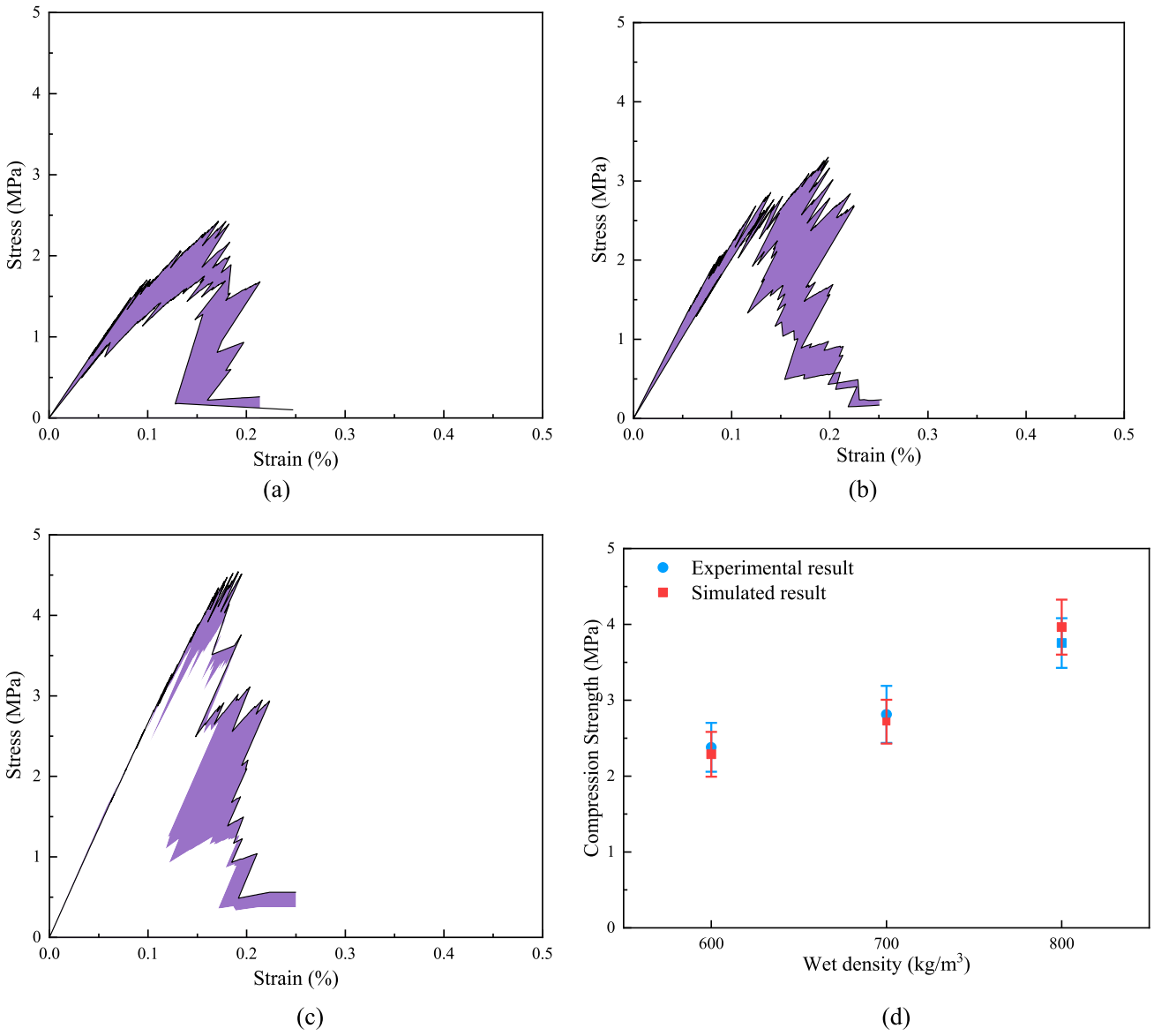

Fig. 14. Simulated results of uniaxial compression about three mixes: (a) M600; (b) M700; (c) M800; (d) Comparison of compressive strength between simulation and experiment.

Table 8
Simulated compressive strength of foamed concrete.

M600		M700		M800	
Porosity (%)	Strength (MPa)	Porosity (%)	Strength (MPa)	Porosity (%)	Strength (MPa)
35.56	2.42	29.90	3.20	21.59	4.52
35.62	1.97	30.09	3.24	22.33	4.47
36.20	2.35	30.17	2.67	23.91	4.38
37.11	1.74	30.28	3.09	24.70	3.95
37.44	2.09	30.55	2.92	24.71	3.96
37.86	1.96	30.93	3.15	24.81	4.07
37.88	2.22	30.93	2.87	25.03	4.02
38.56	2.24	30.94	2.98	25.20	3.99
38.57	1.88	31.07	2.62	25.71	4.24
39.18	1.85	31.07	2.59	25.78	4.12

Table 9
Simulated elastic modulus of foamed concrete.

M600		M700		M800	
Porosity (%)	Elastic modulus (GPa)	Porosity (%)	Elastic modulus (GPa)	Porosity (%)	Elastic modulus (GPa)
35.56	1.77	29.90	2.14	21.59	2.73
35.62	1.57	30.09	2.06	22.33	2.78
36.20	1.64	30.17	2.10	23.91	2.82
37.11	1.72	30.28	2.12	24.70	2.73
37.44	1.24	30.55	2.03	24.71	2.69
37.86	1.43	30.93	1.79	24.81	2.64
37.88	1.47	30.93	1.78	25.03	2.47
38.56	1.29	30.94	1.97	25.20	2.48
38.57	1.55	31.07	1.87	25.71	2.63
39.18	1.12	31.07	1.73	25.78	2.34

compression, splitting tension and three-point bending tests are shown in Fig. 10. The computational uniaxial compression test was performed by applying nodal displacement at one end and fixing the other. In order to consider the horizontal restriction imposed by the steel plates, lateral deformation and rotation at both ends are not allowed.

In terms of the computational Brazilian splitting test, a vertical displacement was applied on 10 nodes closest to the middle axis on both

Table 10
Summary of simulated uniaxial compression test.

Mix	Porosity (%)	Compressive strength (MPa)	Elastic modulus (GPa)
M600	37.40 ± 1.27	2.07 ± 0.23	1.48 ± 0.21
M700	30.59 ± 0.45	2.93 ± 0.24	1.96 ± 0.16
M800	24.37 ± 1.39	4.17 ± 0.22	2.63 ± 0.15

Note: the data in table is addressed as: average ± standard deviation (variation coefficient).

top and bottom ends (Fig. 10b). Regarding the computational three-point bending test, only the material within the two supports (span length: 100 mm) was considered in the model. A vertical displacement was applied on 10 nodes close to the middle axis on the top and 10 nodes at both side of the bottom end were fixed (Fig. 10c).

4. 4.Results and discussion

4.1. Experimental results

The experimentally measured mechanical properties of three mixes are listed in Table 7. In particular, the compressive strength varies from 2.05 to 2.70 MPa for M600, while that of samples of M700 and M800 are in the range of 2.44 to 3.24 MPa and 3.43 to 4.08 MPa, respectively. The variations are attributed to the heterogeneity of the material structure. The average compressive strength of M600 is equal to 2.30 MPa, which is 0.56 MPa and 1.44 MPa lower than M700 and M800. The average splitting strength was 0.35 MPa, 0.48 MPa and 0.57 MPa for M600, M700 and M800, respectively. The mean splitting strength of M800 is 18.75 % and 62.85 % higher than M700 and M600, respectively. The three-point bending strength were 0.522 to 0.728 MPa for M600, 0.804 to 1.011 MPa for M700 and 1.103 to 1.372 MPa for M800.

In terms of the prepared foamed concrete, the ratio of splitting tensile to compressive strength ($\alpha_{sc} = f_s/f_c$) varies between 0.151 and 0.168, while the ratio of three-point bending to compressive strength ($\alpha_{tc} = f_t/f_c$) varies between 0.26 and 0.36 for different mixes, as shown in Fig. 11. For conventional concrete, the splitting tensile to compressive strength ratio is generally in between 0.07 and 0.17 [77–79], and flexural to compressive strength ratio is about 0.12 [80]. They are much lower than the foamed concrete. The relationships between tensile and compressive strength of conventional concrete does not apply for the foamed concrete. This may be attributed by the high porosity and large pore size features of the foamed concrete.

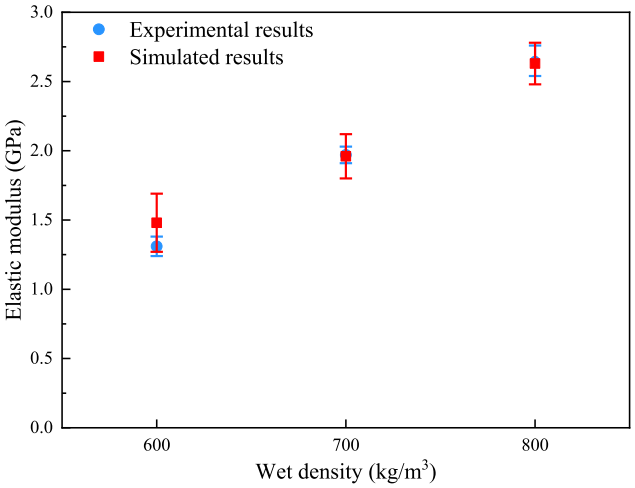

Fig. 16. Comparison of elastic modulus between simulation and experiment.

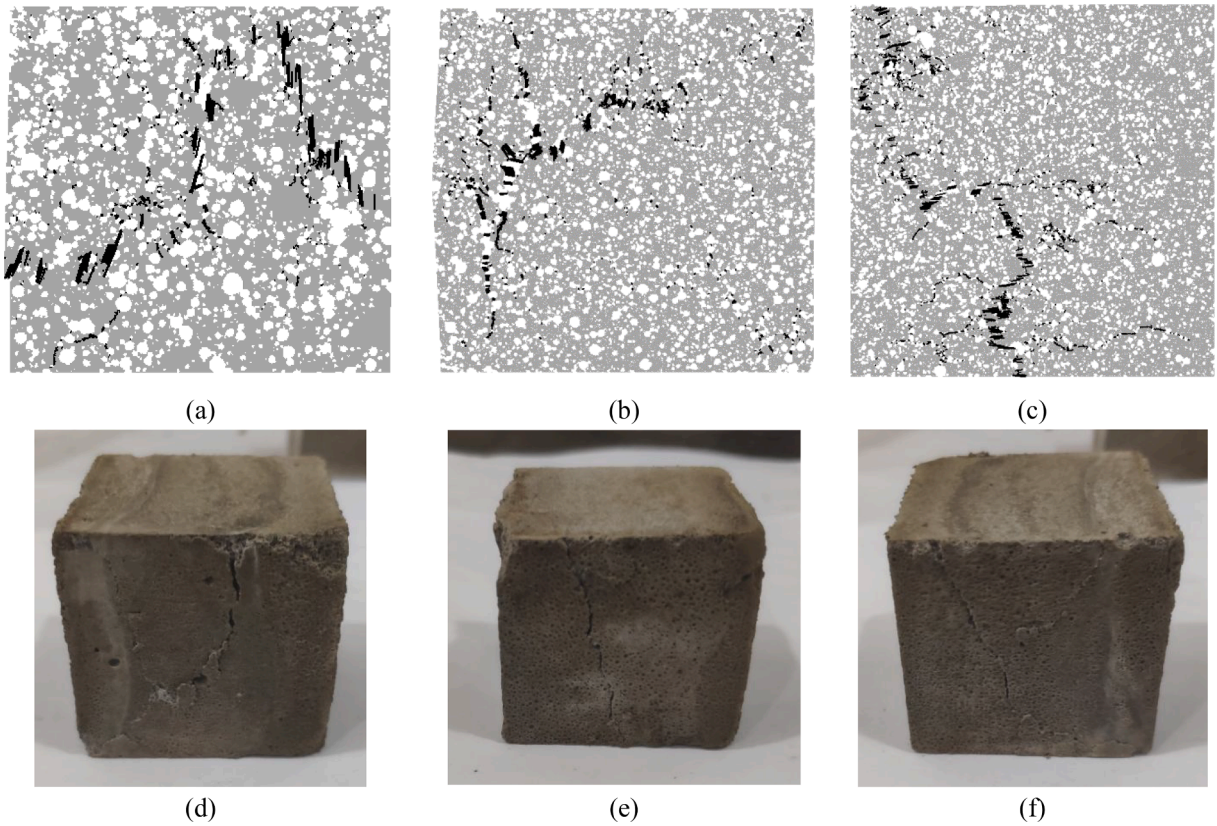

Fig. 15. Comparison of the final fracture pattern about uniaxial compression with three mixes: (a) M600; (b) M700; (c) M800 of simulated result; (d) M600; (e) M700; (d) M800 of experimental result.

Table 11
Simulated Brazilian splitting strength of foamed concrete.

M600		M700		M800	
Porosity (%)	Strength (MPa)	Porosity (%)	Strength (MPa)	Porosity (%)	Strength (MPa)
39.70	0.29	30.19	0.46	25.71	0.55
37.71	0.32	30.93	0.50	25.03	0.65
36.23	0.28	30.28	0.45	23.91	0.52
38.46	0.27	30.93	0.56	25.78	0.60
36.10	0.32	31.20	0.52	24.81	0.59
39.07	0.32	31.07	0.49	24.70	0.70
39.06	0.35	29.85	0.57	21.59	0.63
37.85	0.38	30.15	0.52	22.33	0.71
36.70	0.32	30.93	0.48	25.20	0.57
38.38	0.31	30.64	0.55	24.71	0.61

4.2. Modelling results

4.2.1. Influence of input parameters on simulated results

M700 was used to investigate the effect of input parameters on the simulated results. The simulated stress-displacement responses and experimental results are compared in Fig. 12. The shaded areas are taken from 10 models using the upper and lower limits. Note that experiments were ran in load control and only the maximum force (stress) was measured, so it is not possible to compare full load–displacement curves between the experiments and the simulations. It can be found that the predicted mechanical properties of foamed concrete using Model-I are lower than those obtained using Model-II. Specifically, the simulated average compressive strength, splitting tensile strength and three-point bending strength of Model I are 17.5 %, 8.9 % and 21.8 % lower than those of Model II, respectively. This is mainly attributed to the fact that the mechanical properties following Weibull distribution of elements introduce more defects into the model. The comparison between the two simulated and experimental results is in good agreement.

Fig. 13 compares the crack patterns of the same material structure simulated by Model-I and Model-II. It can be found that the main patterns are the same in general. This can be attributed to the high porosity

Table 12
Summary of Brazilian splitting test.

Mix	Porosity (%)	Splitting strength (MPa)
M600	37.93 ± 1.25	0.32 ± 0.03
M700	30.62 ± 0.46	0.51 ± 0.04
M800	24.38 ± 1.39	0.61 ± 0.06

Note: the data in table is addressed as: average ± standard deviation (variation coefficient).

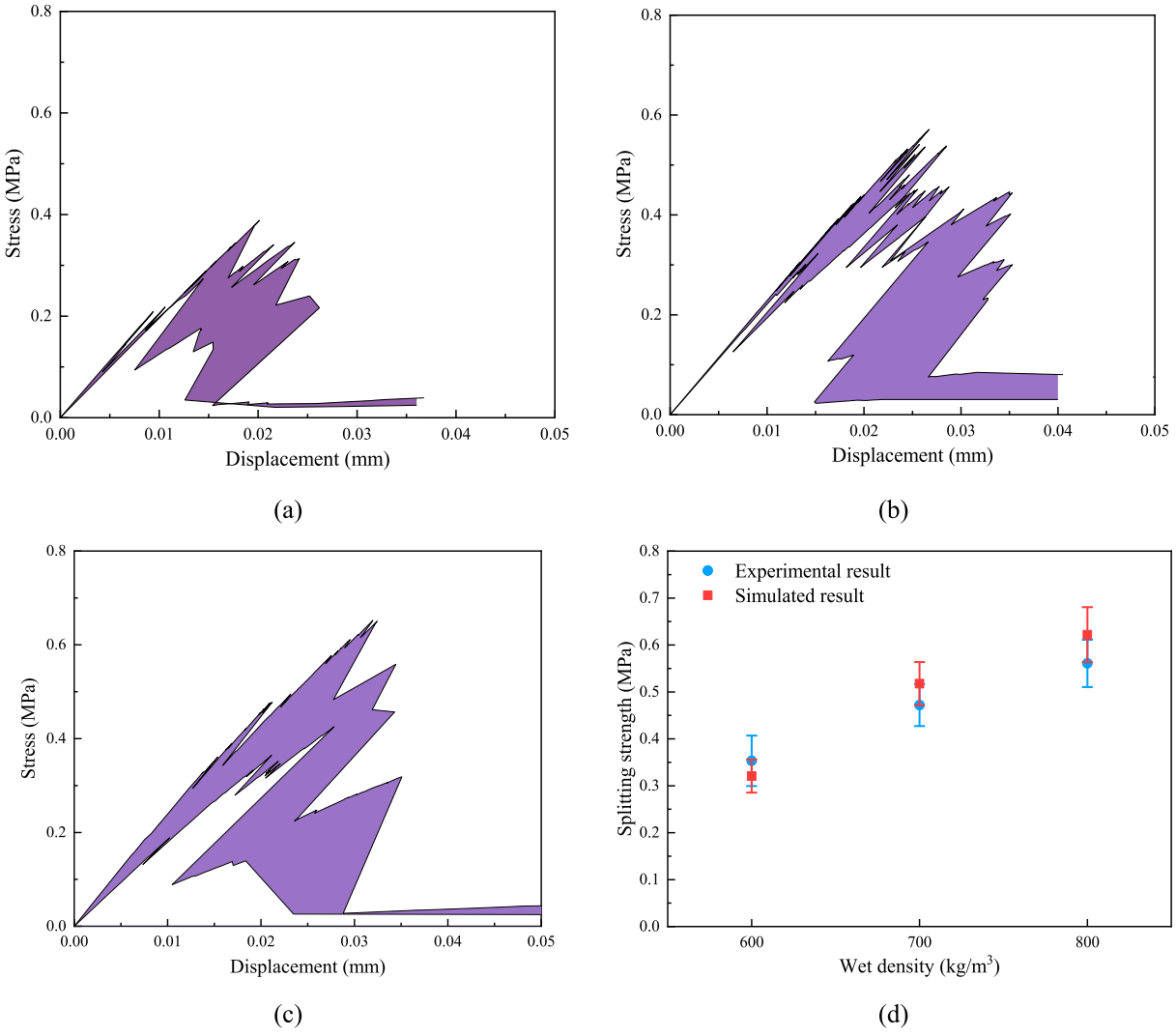

Fig. 17. Simulated results of Brazilian splitting about three mixes: (a) M600; (b) M700; (c) M800; (d) Comparison of compressive strength between simulation and experiment.

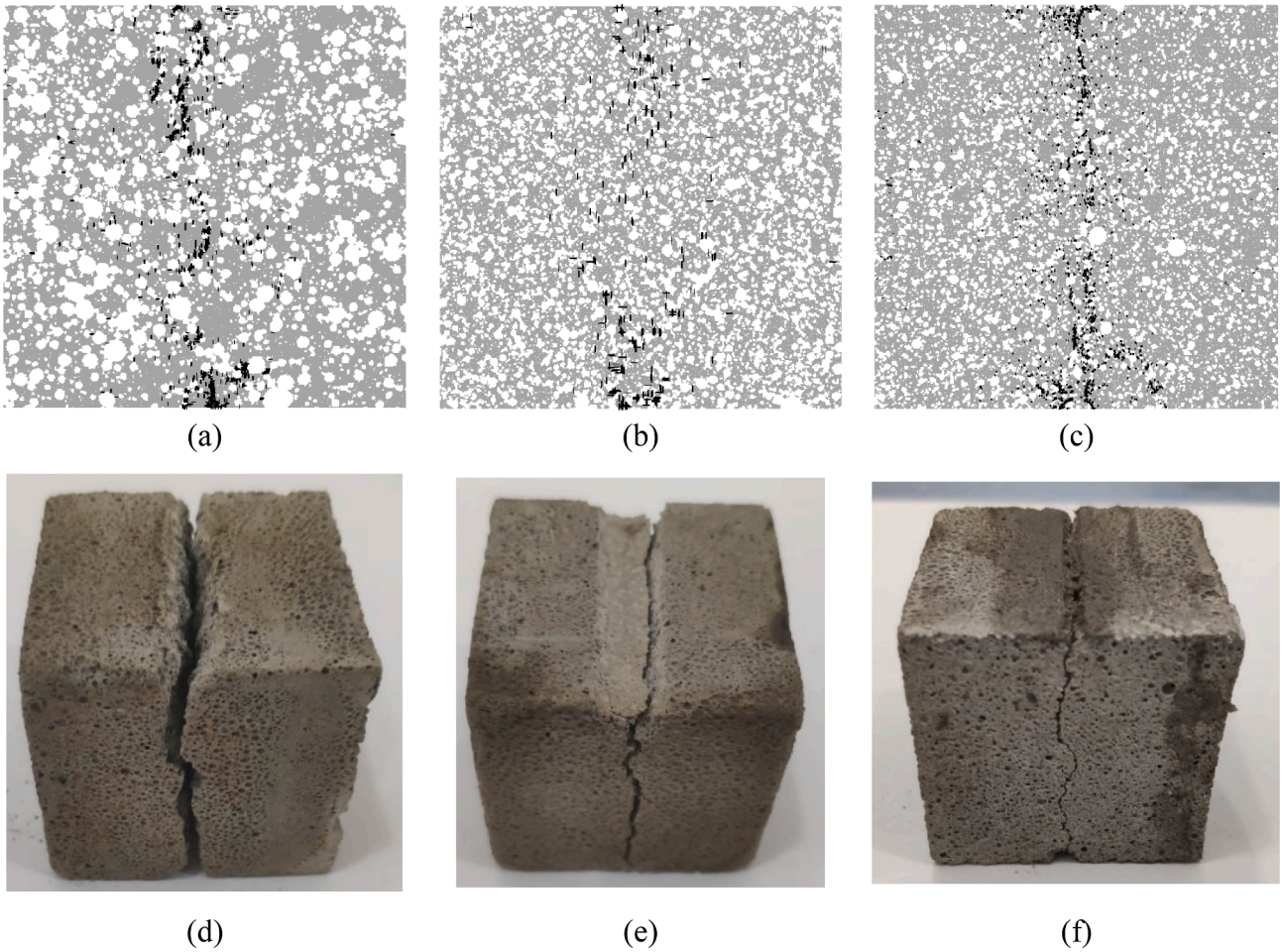

Fig. 18. Comparison of the final fracture pattern about Brazilian splitting with three mixes: (a) M600; (b) M700; (c) M800 of simulated result; (d) M600; (e) M700; (d) M800 of experimental result.

Table 13
Simulated three-point bending strength of foamed concrete.

M600		M700		M800	
Porosity (%)	Strength (MPa)	Porosity (%)	Strength (MPa)	Porosity (%)	Strength (MPa)
36.06	0.83	29.90	1.17	21.61	1.41
36.12	0.71	30.15	1.14	22.33	1.38
36.70	0.74	30.17	1.12	23.96	1.33
37.68	0.73	30.28	1.09	24.76	1.36
37.94	0.61	30.61	1.01	24.71	1.37
38.38	0.65	30.85	0.99	24.81	1.25
38.40	0.67	30.93	1.11	25.03	1.30
39.06	0.56	30.89	1.13	25.28	1.30
39.14	0.59	31.14	0.97	25.74	1.17
39.71	0.51	31.07	0.92	25.69	1.09

of foamed concrete which dominates the crack propagation. Difference can also be observed. Model-I has a more torturous main crack and more failure elements apart from the main crack. This is because that when the properties of local solid element were assumed to follow the Weibull distribution, weak spots were randomly introduced in the solid matrix, which is more realistic. Therefore, Weibull distribution based-input parameters were used for all remaining simulations.

4.2.2. Computational uniaxial compression test

Fig. 14 shows the simulated stress–strain curve of the foamed concrete with different densities. As the foamed concrete density increases, the ultimate load bearing capacity also increases. Similar trends have been reported in previous studies [1,81].This is because more air-voids are formed in the low density mixtures [82]. It also can be explained that there are relatively thicker internal pore walls and more uniform distribution of pores in the foamed concrete with higher wet density. The compressive strengths were calculated from the stress–strain curves and listed in Table 8. The average results of each mix are summarized in Table 10. The initial pore structure of foamed concrete has a significant effect on the compressive behavior of the material, which leads to the variation of the same batch specimen. The average uniaxial compressive strength of M600 is 2.07 MPa, which is 29 % and 50 % lower than that of the M700 and M800, respectively. The compressive strength obtained from the lattice model show good agreement with the experimental results as shown in Fig. 14d. In addition, the standard deviations of experiment and simulation of the three mixes are in good agreement.

Typical crack patterns at failure stage for the three mixes are shown in Fig. 15 for comparison. Cracks tend to arise near the pore surface and propagate along the weaker phases connecting the pores. Tortuous and diagonal main cracks are observed in both experiments and simulation.

The initial slope of the stress–strain curve was used to derive the elastic moduli which are listed in Table 9. Clearly, they show good agreement with the experimental results (Fig. 16). The present study shows that, with carefully design, it is capable of predicting the strength and elastic modulus efficiently.

4.2.3. Computational Brazilian splitting test

The simulated splitting tensile strengths are listed in Table 11 and the stress-displacement curves are plotted in Fig. 17. The splitting strength

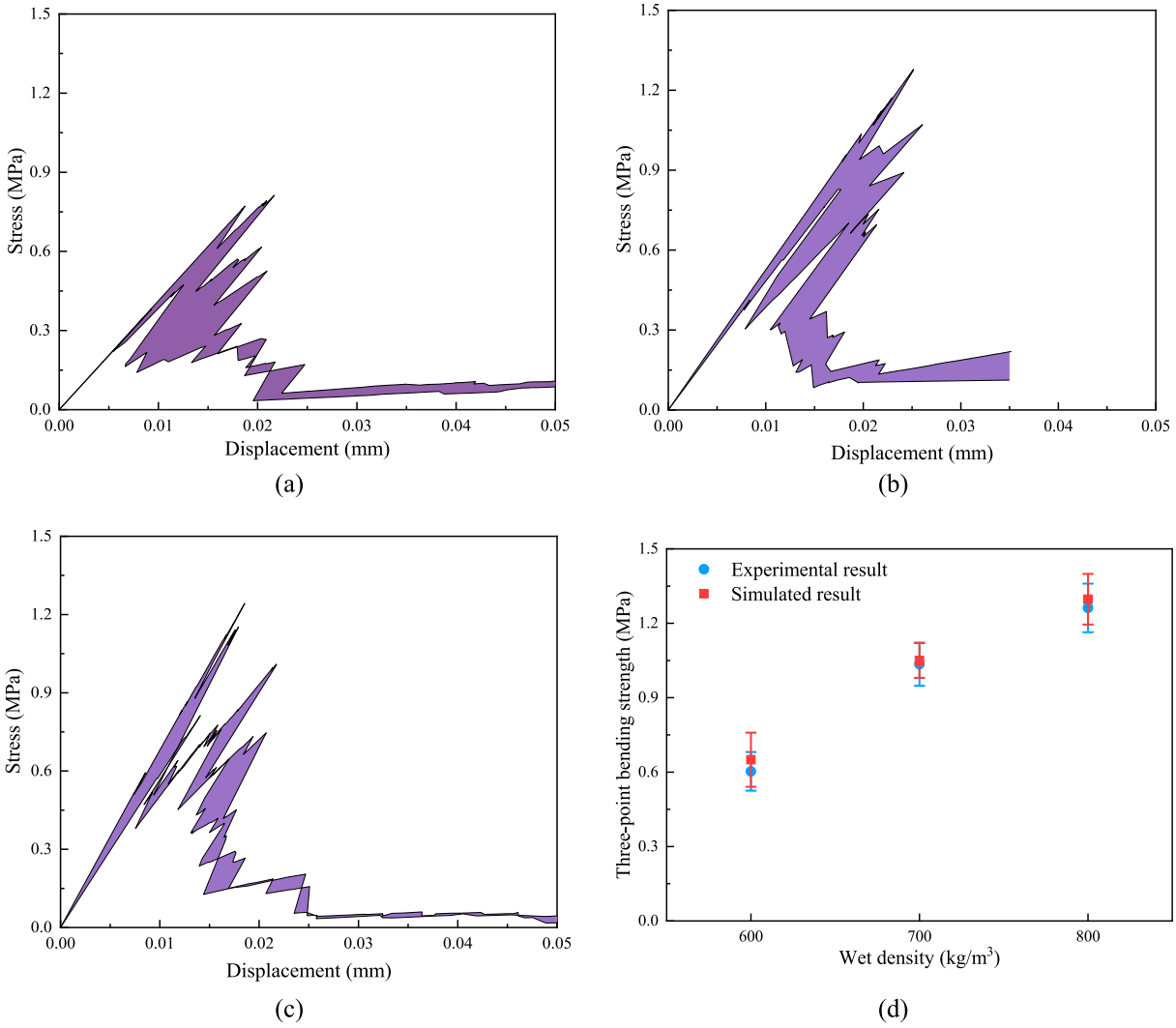

Fig. 19. Simulated results of three-point bending about three mixes: (a)M600; (b) M700; (c) 800; (d) Comparison of compressive strength between simulation and experiment.

Table 14
Summary of three-point bending test.

Mix	Porosity (%)	Three-point bending strength (MPa)
M600	37.92 ± 1.28	0.65 ± 0.11
M700	30.60 ± 0.44	1.05 ± 0.07
M800	24.39 ± 1.39	1.30 ± 0.10

Note: the data in table is addressed as: average ± standard deviation (variation coefficient).

of three mixes were 0.27 to 0.38 MPa for M600, 0.45 to 0.57 MPa for M700 and 0.52 to 0.71 MPa for M800. As discussed in the previous section, it can be explained that the predicted results show a certain degree of variability, which is caused by the inherent heterogeneity of the material in this length range. The comparison of splitting strength between simulation and experiment is observed in Fig. 17d. The splitting strengths obtained from the simulation are well in agreement with experiment. The average results of each mix are summarized in Table 12. It can be easily seen that the average of the simulated results for the three mixes differs from the experimental results within 10 %: while the strength of M600 from experiment is a bit higher than that from simulation, the opposite is observed for M700 and M800. Similar to the compressive strength, the Brazilian splitting strength of foamed concrete decreases with an increase in foam volume content.

The simulated crack patterns at failure stage are compared in Fig. 18. It is evident that, the specimen was split in half along the line of concentrated load, although some local cracks appeared around the crack tip and pores due to stress concentration. This is consistent with the experimental observations as shown in Fig. 18. Similar fracture pattern can also be observed in conventional concrete [83,84].

4.2.4. *Computational three-point bending test*

The simulated three-point bending strengths are listed in Table 13. It is observed that the average strength value was 0.65, 1.05 and 1.30 MPa for M600, M700 and M800, respectively. The strength increases with the density. Fig. 19 presents the simulated stress-displacement curves. Comparisons between experimental and simulated results are displayed in Fig. 19d. The average strengths of each mix are summarized in.

Table 14. The simulated average strength was 7 % for M600, 1 % for M700 and 3 % for M800 higher than the experiments, respectively. Good agreements are found between simulation (red curve) and experiment results (blue curve).

The simulated and experimental fracture patterns at failure stage are compared in Fig. 20. The three mixes simulation show similar main cracks. Although the crack propagated tortuously around the randomly distributed pores, it eventually moved towards from the bottom of specimen to the upper along the top loading point. Furthermore, it can be clearly seen that the crack patterns between the simulation and

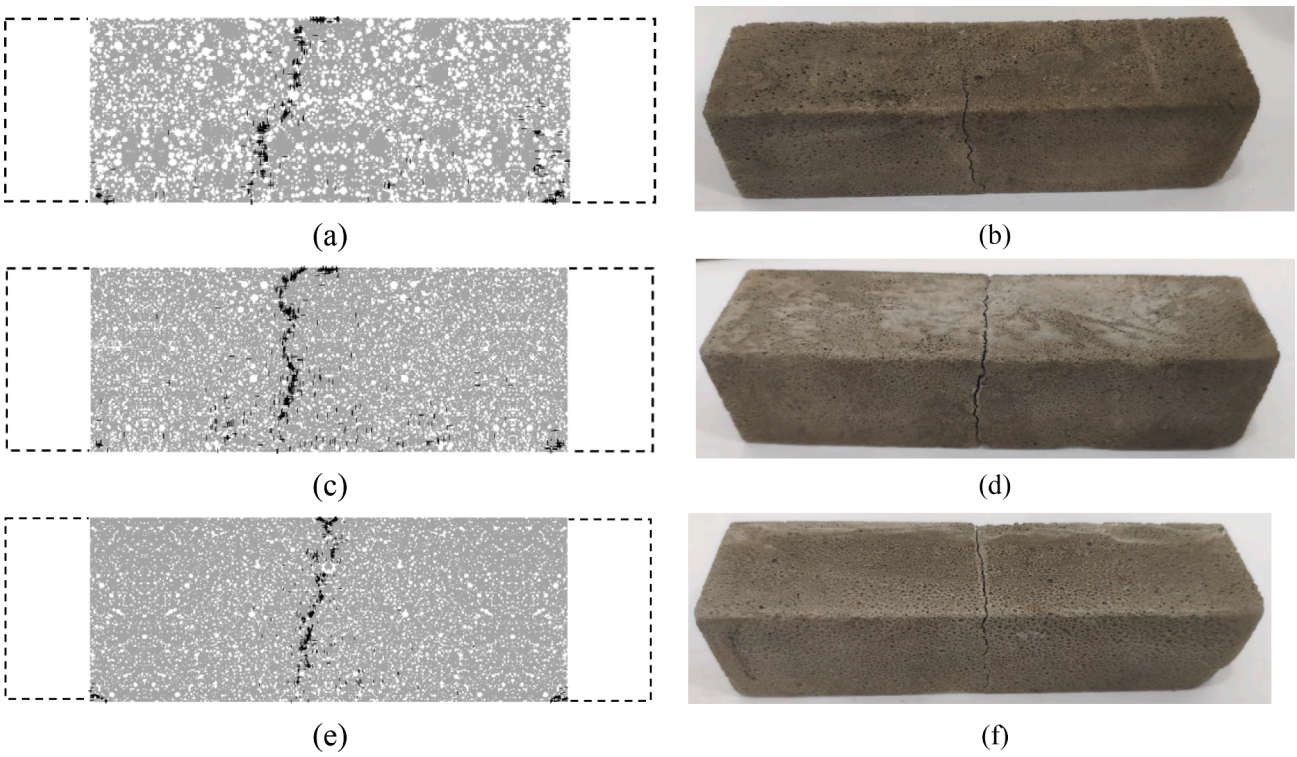

Fig. 20. Comparison of the final fracture pattern about three-point bending with three mixes: M600 crack pattern: (a) simulation (b) experiment; M700 crack pattern: (c) simulation; (d) experiment; M800 crack pattern: (e) simulation; (f) experiment.

Table 15
The K_{IC} of different mix.

M600	M700	M800			
Porosity (%)	Fracture toughness (MPa $\sqrt{m}$)	Porosity (%)	Fracture toughness (MPa $\sqrt{m}$)	Porosity (%)	Fracture toughness (MPa $\sqrt{m}$)
36.06	0.078	29.90	0.083	21.61	0.094
36.12	0.067	30.15	0.081	22.33	0.092
36.70	0.070	30.17	0.079	23.96	0.089
37.68	0.069	30.28	0.077	24.76	0.091
37.94	0.058	30.61	0.072	24.71	0.091
38.38	0.061	30.85	0.070	24.81	0.083
38.40	0.063	30.93	0.079	25.03	0.087
39.06	0.053	30.89	0.080	25.28	0.087
39.14	0.056	31.14	0.069	25.74	0.078
39.71	0.048	31.07	0.065	25.69	0.073

Table 16
Summary of fracture toughness.

Mix	Average three-point bending strength (MPa)	Average pore diameter (μm)	Fracture toughness (MPa $\sqrt{m}$)
M600	0.65 ± 0.11	744.33	0.061 ± 0.009
M700	1.05 ± 0.07	419.47	0.074 ± 0.006
M800	1.30 ± 0.10	371.55	0.087 ± 0.006

experiment show a good agreement.

It is observed that the flexural strength is about twice of the splitting strength, indicating the fracture toughness is low. For brittle homogeneous materials, the fracture toughness K_{IC}, defined by Linear Elastic Fracture Mechanics (LEFM), is a key material property for crack initiation and propagation, and therefore should be considered for foamed concrete [85]. K_{IC}, is typically measured according to the ASTM standard [86] using specimens with initial notches/cracks. It is also considered to be independent of the tensile strength f_t. Hu et al. [87] connected these two fundamental properties using fracture process zone width at the peak fracture load. The K_{IC} can be calculated by the following Eq. (4) [88,89].

$$K_{IC} = 2f_t\sqrt{3C_{ch}} \tag{4}$$

Where f_t. is the flexural strength and C_{ch} is the characteristic microstructure of the material. In this study, the average pore diameter was considered as C_{ch}. The calculated K_{IC} of each specimen is listed in Table 15. The average of K_{IC} is shown in Table 16. Compared with a light-weight foam concrete prepared with weak aggregates [90] whose fracture toughness K_{IC} is 0.35 MPa $\sqrt{m}$, the studied foamed concretes possess much lower K_{IC} (0.061–0.087 MPa $\sqrt{m}$). It is mainly due to the high porosity of foamed concrete. As it has found that the toughness of conventional concrete [91] and mortar [92] is 1.46–1.80 MPa $\sqrt{m}$ and 0.81–0.86 MPa $\sqrt{m}$, respectively. They are significantly higher than the light weight concrete present in [90]. It shows that the pore increases the brittleness of the material, and thus reduces the fracture toughness. The low fracture toughness further explained the very low splitting strength observed in this study.

4.3. Relationship between porosity and mechanical properties

In foamed concrete, pores act as stress concentration sites and promote failure under loading by introducing stress concentration. Hence, an increase in pore volume reduces the elastic modulus and strength of the material [4]. The shape, size and position of pores are all parameters affecting the deformation and fracture properties [93]. Among those, porosity is regarded as the governing parameter for mechanical properties of foamed concrete [14,16,18]. Although many efforts have been made to correlate strength with porosity for foamed concrete [13,81], few of them have focused on the splitting strength or three-point bending strength. With respect to porous materials, quite a few equations have been proposed and developed for expressing the effect of

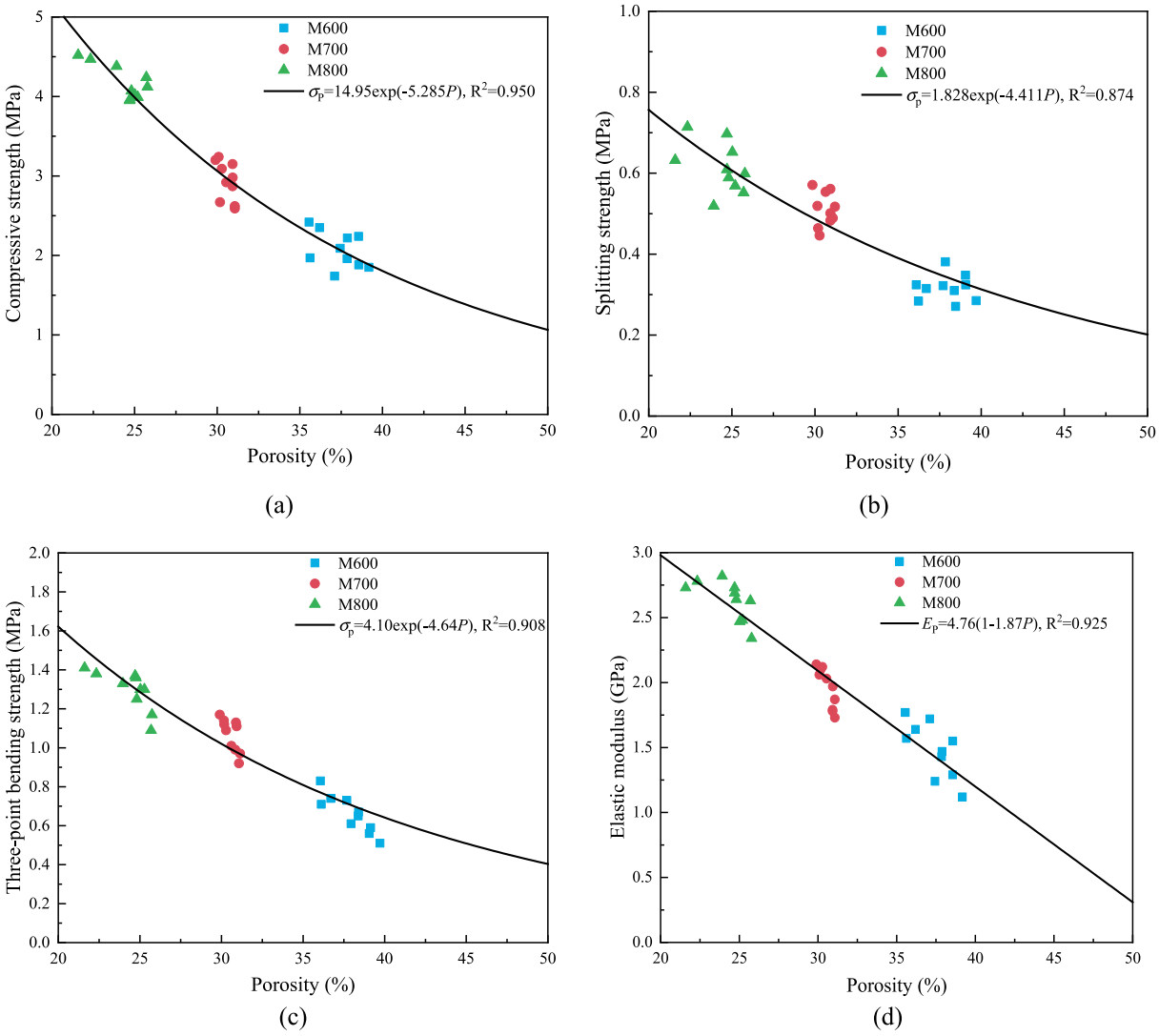

Fig. 21. Relationship between predicted mechanical properties and porosity: (a) compressive strength-porosity; (b) splitting strength-porosity; (c) three-point bending strength-porosity; (d) elastic modulus-porosity.

porosity on strength and elastic modulus [94–99]. The fitted strength–porosity and modulus–porosity relations are given in Fig. 21.

In the current study, an exponential function ($\sigma_p = \sigma_0\, e^{-kfP}$) [94] was used to characterize the strength-porosity relation, in which σ_p stands for strength at porosity P, σ_0 stands for strength at zero porosity, k_f is an empirical constant fitted from the simulated results. For elastic modulus, the fitting with the porosity was achieved with the linear function of ($E_p = E_0\,(1\text{-}k_eP)$) [95], in which E_p denotes elasticity modulus at porosity P, E_0 is the elasticity modulus at zero porosity, k_f is an empirical constant need to be fitted. The determination coefficient of the fitting is relatively high for all cases. The fitted model predicts the compressive strength, splitting strength, three-point bending strength and elastic modulus are 14.95 MPa, 1.83 MPa, 4.1 MPa and 1.76 GPa, respectively, when the porosity tends towards 0. And as the porosity equal to 1, an elastic modulus of −4.14 GPa was predicted. Clearly, the aforementioned predictions are not realistic. Hence, one should be careful with how these fitted parameters are used in practical applications beyond the tested range. In order to improve the accuracy of the fitted function, it is necessary to broaden the simulated results of specimens with porosity lower than 20 % and higher than 40 %. This can be done by applying the computational uniaxial compression, splitting tension and three-point bending tests on the specimens with broader porosity range.

5. Conclusions

The current study presents experimentally-informed discrete lattice modelling of foamed concrete at the meso-scale. Two phases, namely pore and hydrated cement paste were considered. The XCT and image segmentation techniques were used to build the microstructure of foamed concrete. A discrete lattice was used for the fracture process modelling. The properties of hydrated cement paste were derived from micro-scale modelling and assigned to the lattice element. It is shows that the adopted modelling strategy can predict the mechanical properties (e.g., compressive strength, splitting tensile strength, three-point bending strength and elastic modulus) and crack pattern satisfactorily without further calibration. The following conclusions can be drawn:

- The pore diameter mainly concentrates in the range of 0.2 mm and 0.8 mm, which accounts for more than 50 % of the total pore for all three mixes. The average pore diameter of foamed concrete decreases along with the increasing wet density. The number of pores with a spacing less than 150 μm reaches more than 50 % in all three mixes.
- In terms of the same material structure, Model-I predicts a smaller strength and more torturous crack than Model-II due to the fact that the local mechanical properties of hydrated cement paste following

Weibull distribution introducing weak points into the model, which is more realistic.

- The strength and elastic modulus increase along with the density in both experiments and simulations. The comparison between experiment and simulation proves that the adopted modelling strategy is capable of predicting the mechanical properties and fracture behavior of foamed concrete under various boundary conditions.
- The fracture toughness K_{IC} is obtained using three-point bending strength and the average pore diameter. It shows that the existence of pore increases the brittleness of the foamed concrete and decreases the fracture toughness. The low fracture toughness explains the very low splitting strength.
- Over the examined porosity of foamed concrete, ranging from 20 % to 40 %, the exponential function and linear function can be regarded as good representation for strength–porosity and modulus–porosity relationships, respectively. However, the estimated mechanical properties are not reliable with porosity towards 0 and 100 %.

CRediT authorship contribution statement

Nengdong Jiang: Investigation, Writing – original draft. **Zhi Ge:** Funding acquisition, Writing – review & editing. **Yanhua Guan:** Writing – review & editing. **Zhiwu Zuo:** Writing – review & editing. **Hongzhi Zhang:** Funding acquisition, Methodology, Supervision, Writing – review & editing. **Yifeng Ling:** Funding acquisition, Supervision, Writing – review & editing. **Branko Šavija:** Methodology, Writing – review & editing.

Declaration of Competing Interest

The authors declare that they have no known competing financial interests or personal relationships that could have appeared to influence the work reported in this paper.

Data availability

Data will be made available on request.

Acknowledgments

This work was supported by the National Natural Science Foundation of China (No. 52008234, 51978387), Taishan Scholars Foundation of Shandong Province (No. tsqn201909032), Natural Science Foundation of Jiangsu Province (No. BK20200235) and Natural Science Foundation of Shandong Province (No. ZR2021QE174)

References

[1] K. Ramamurthy, E.K. Nambiar, G.I.S.J.C. Ranjani, c. composites, A classification of studies on properties of foam concrete 31 (2009) 388–396.
[2] A. Raj, D. Sathyan, K.J.C. Mini, B. Materials, Physical and functional characteristics of foam concrete: A review 221 (2019) 787–799.
[3] Y.M. Amran, N. Farzadnia, A.A.J.C. Ali, B. Materials, Properties and applications of foamed concrete; a review 101 (2015) 990–1005.
[4] Z. Ge, H. Yuan, R. Sun, H. Zhang, W. Wang, H.J.C. Qi, B. Materials, Use of green calcium sulphoaluminate cement to prepare foamed concrete for road embankment: A feasibility study 237 (2020), 117791.
[5] Y.M. Amran, R. Alyousef, H. Alabduljabbar, M. Khudhair, F. Hejazi, A. Alaskar, F. Alrshoudi, A.J.R.i.E. Siddika, Performance properties of structural fibred-foamed concrete 5 (2020), 100092.
[6] N. Mohamad, W. Omar, R.J.O.I.J.o.S.D. Abdullah, Structural behaviour of precast lightweight foamed concrete sandwich panel as a load bearing wall 5 (2012) 49–58.
[7] K. Wu, Z. Shao, S. Qin, A solution for squeezing deformation control in tunnels using foamed concrete: A review, Construction and Building Materials 257 (2020), 119539.
[8] A. Tarasov, E.P. Kearsley, A. Kolomatskiy, H.J.M.o.c.r. Mostert, Heat evolution due to cement hydration in foamed concrete 62 (2010) 895–906.
[9] M. Jones, A. McCarthy, Behaviour and assessment of foamed concrete for construction applications, in: Use of foamed concrete in construction: Proceedings of the international conference held at the University of Dundee, Scotland, UK on 5 July 2005, Thomas Telford Publishing, 2005, pp. 61-88.
[10] P. Gao, Y. Chen, H. Huang, Z. Qian, E. Schlangen, J. Wei, Q.J.C. Yu, C. Composites, Investigation of drying-induced non-uniform deformation, stress, and micro-crack propagation in concrete 114 (2020), 103786.
[11] P.J. Tikalsky, J. Pospisil, W.J.C. MacDonald, c. research, A method for assessment of the freeze–thaw resistance of preformed foam cellular concrete 34 (2004) 889–893.
[12] D. Falliano, D. De Domenico, G. Ricciardi, E.J.C. Gugliandolo, B. Materials, Experimental investigation on the compressive strength of foamed concrete: Effect of curing conditions, cement type, foaming agent and dry density 165 (2018) 735–749.
[13] E.K. Nambiar, K.J.C. Ramamurthy, C. Composites, Models relating mixture composition to the density and strength of foam concrete using response surface methodology 28 (2006) 752–760.
[14] M.J.C. Zhang, C. Research Pore-scale modelling of relative permeability of cementitious materials using X-ray computed microtomography images 95 (2017) 18–29.
[15] S.-Y. Chung, J.-S. Kim, T.-S.-J.-M.-S. Han, Engineering, Effects of void clustering on the thermal and mechanical properties of concrete evaluated using numerical methods 1 (2019) 196–209.
[16] T.-H. Wee, D.S. Babu, T. Tamilselvan, H.-S.J.A.m.j. Lim, Air-void system of foamed concrete and its effect on mechanical properties 103 (2006) 45.
[17] A.A. Hilal, N.H. Thom, A.R.J.C. Dawson, B. Materials, On entrained pore size distribution of foamed concrete 75 (2015) 227–233.
[18] A.A. Hilal, N.H. Thom, A.R.J.C. Dawson, B. Materials, On void structure and strength of foamed concrete made without/with additives 85 (2015) 157–164.
[19] S. Zhuang, Q.J.C. Wang, C. Research, Inhibition mechanisms of steel slag on the early-age hydration of cement 140 (2021), 106283.
[20] Y. Guo, X. Chen, B. Chen, R. Wen, P.J.C. Wu, B. Materials, Analysis of foamed concrete pore structure of railway roadbed based on X-ray computed tomography 273 (2021), 121773.
[21] T.T. Nguyen, H.H. Bui, T.D. Ngo, G.D. Nguyen, M.U. Kreher, F. Darve, A micromechanical investigation for the effects of pore size and its distribution on geopolymer foam concrete under uniaxial compression, Engineering Fracture Mechanics 209 (2019) 228–244.
[22] E.K. Nambiar, K.j.c. Ramamurthy, c. research, Air-void characterisation of foam concrete 37 (2007) 221–230.
[23] E. Kuzielová, L. Pach, M.J.C. Palou, B. Materials, Effect of activated foaming agent on the foam concrete properties 125 (2016) 998–1004.
[24] S. Wei, C. Yiqiang, Z. Yunsheng, M.J.C. Jones, b. materials,Characterization and simulation of microstructure and thermal properties of foamed concrete 47 (2013) 1278–1291.
[25] H.S. Wong, M.K. Head, N.R. Buenfeld, Pore segmentation of cement-based materials from backscattered electron images, Cement and Concrete Research 36 (2006) 1083–1090.
[26] H. Lu, E. Alymov, S. Shah, K. Peterson, Measurement of air void system in lightweight concrete by X-ray computed tomography, Construction and Building Materials 152 (2017) 467–483.
[27] A. Hajimohammadi, T. Ngo, P. Mendis, J. Sanjayan, Regulating the chemical foaming reaction to control the porosity of geopolymer foams, Materials & Design 120 (2017) 255–265.
[28] M.B. Youssef, F. Lavergne, K. Sab, K. Miled, J. Neji, Upscaling the elastic stiffness of foam concrete as a three-phase composite material, Cement and Concrete Research 110 (2018) 13–23.
[29] W. She, Y. Du, C. Miao, J. Liu, G. Zhao, J. Jiang, Y. Zhang, Application of organic- and nanoparticle-modified foams in foamed concrete: Reinforcement and stabilization mechanisms, Cement and Concrete Research 106 (2018) 12–22.
[30] E. Schlangen, E.J.J.E.f.m., Garboczi, Fracture simulations of concrete using lattice models: computational aspects 57 (1997) 319–332.
[31] E. Schlangen, J.J.M. Van Mier, Structures, Simple lattice model for numerical simulation of fracture of concrete materials and structures 25 (1992) 534–542.
[32] M. Nitka, J.J.G.M. Tejchman, Modelling of concrete behaviour in uniaxial compression and tension with DEM 17 (2015) 145–164.
[33] Q.-S. Bai, S.-H. Tu, C.J.T. Zhang, A.F. Mechanics, DEM investigation of the fracture mechanism of rock disc containing hole (s) and its influence on tensile strength, 86 (2016) 197-216.
[34] P.A. Cundall, O.D.J.g. Strack, A discrete numerical model for granular assemblies 29 (1979) 47–65.
[35] P. Wriggers, S.J.F.e.i.a. Moftah, design, Mesoscale models for concrete: Homogenisation and damage behaviour 42 (2006) 623–636.
[36] E.A. Rodrigues, O.L. Manzoli, L.A. Bitencourt Jr, T.N.J.I.J.o.S. Bittencourt, Structures, 2D mesoscale model for concrete based on the use of interface element with a high aspect ratio 94 (2016) 112–124.
[37] G. Lilliu, J.G.M. van Mier, 3D lattice type fracture model for concrete 70 (2003) 927–941.
[38] Y. Feng D.J.E.C. Owen A, 2D polygon/polygon contact model: algorithmic aspects 2004.
[39] H. Guo, E. Ooi, A. Saputra, Z. Yang, S. Natarajan, E. Ooi, C.J.E.F.M. Song, A quadtree-polygon-based scaled boundary finite element method for image-based mesoscale fracture modelling in concrete 211 (2019) 420–441.
[40] J. Suchorzewski, J. Tejchman, M.J.I.J.o.D.M. Nitka, Discrete element method simulations of fracture in concrete under uniaxial compression based on its real internal structure 27 (2018) 578–607.
[41] W.H. Gerstle, M.J.J.o.E.M. Xie, FEM modeling of fictitious crack propagation in concrete 118 (1992) 416–434.

[42] M. Nitka, J.J.E.f.m. Tejchman, Modelling of concrete fracture at aggregate level using FEM and DEM based on X-ray μCT images of internal structure 147 (2015) 13–35.
[43] A. Yaghoobi, M.G. Chorzepa, S.S. Kim, S.A.J.M. Durham, Mesoscale fracture analysis of multiphase cementitious composites using peridynamics 10 (2017) 162.
[44] C.M. López, I. Carol, A.J.M. Aguado, structures, Meso-structural study of concrete fracture using interface elements. I: numerical model and tensile behavior, 41 (2008) 583-599.
[45] L. Snozzi, F. Gatuingt, J.-F.J.I.j.o.f. Molinari, A meso-mechanical model for concrete under dynamic tensile and compressive loading 178 (2012) 179–194.
[46] N. Benkemoun, P. Poullain, H. Al Khazraji, M. Choinska, A.J.E.f.m. Khelidj, Meso-scale investigation of failure in the tensile splitting test: Size effect and fracture energy analysis, 168 (2016) 242-259.
[47] S. Shahbeyk, M. Hosseini, M.J.C.M.S. Yaghoobi, Mesoscale finite element prediction of concrete failure 50 (2011) 1973–1990.
[48] X. Du, L. Jin, G.J.I.J.o.D.M. Ma, Numerical modeling tensile failure behavior of concrete at mesoscale using extended finite element method 23 (2014) 872–898.
[49] I. Viejo, L.P. Esteves, M. Laspalas, J.M. Bielsa, Numerical modelling of porous cement-based materials by superabsorbent polymers, Cement and Concrete Research 90 (2016) 184–193.
[50] T. Nguyen, A. Ghazlan, A. Kashani, S. Bordas, T. Ngo, 3D meso-scale modelling of foamed concrete based on X-ray Computed Tomography, Construction and Building Materials 188 (2018) 583–598.
[51] J.-S. Kim, S.-Y. Chung, T.-S. Han, D. Stephan, M.J.C. Abd Elrahman, C., Composites, Correlation between microstructural characteristics from micro-CT of foamed concrete and mechanical behaviors evaluated by experiments and simulations 112 (2020), 103657.
[52] T.T. Nguyen, H.H. Bui, T.D. Ngo, G.D.J.M. Nguyen, Design, Experimental and numerical investigation of influence of air-voids on the compressive behaviour of foamed concrete 130 (2017) 103–119.
[53] H. Zhang, B. Šavija, Y. Xu, E.J.C. Schlangen, C. Composites, Size effect on splitting strength of hardened cement paste: Experimental and numerical study 94 (2018) 264–276.
[54] H.K. Man, J.G.M. van Mier, Damage distribution and size effect in numerical concrete from lattice analyses, Cement and Concrete Composites 33 (2011) 867–880.
[55] H.-K. Man, J.G.J.I.j.o.f. van Mier, Size effect on strength and fracture energy for numerical concrete with realistic aggregate shapes 154 (2008) 61–72.
[56] E.K.K. Nambiar, K. Ramamurthy, Air-void characterisation of foam concrete, Cement and Concrete Research 37 (2007) 221–230.
[57] H. Zhang, B. Šavija, E.J.C. Schlangen, B. Materials, Towards understanding stochastic fracture performance of cement paste at micro length scale based on numerical simulation 183 (2018) 189–201.
[58] N. Bossa, P. Chaurand, J. Vicente, D. Borschneck, C. Levard, O. Aguerre-Chariol, J. Rose, Micro- and nano-X-ray computed-tomography: A step forward in the characterization of the pore network of a leached cement paste, Cement and Concrete Research 67 (2015) 138–147.
[59] J.-S. Kim, S.-Y. Chung, D. Stephan, T.-S. Han, Issues on characterization of cement paste microstructures from μ-CT and virtual experiment framework for evaluating mechanical properties, Construction and Building Materials 202 (2019) 82–102.
[60] J.-S. Kim, S.-Y. Chung, T.-S. Han, D. Stephan, M.J.C. Abd Elrahman, B. Materials, Modeling of multiple phase solid microstructures and prediction of mechanical behaviors of foamed concrete 248 (2020), 118637.
[61] F. Rao, Z. Zhang, G. Ye, J. Liu, J. J. J. o.M.i.C.E. Han, Mesostructure of foamed cement paste and its influence on macromechanical behavior 33 (2021) 04021114.
[62] H. Dong, P. Gao, G.J.M. Ye, Structures, Characterization and comparison of capillary pore structures of digital cement pastes 50 (2017) 1–12.
[63] H. Dong, H. Zhang, Y. Zuo, P. Gao, G.J.M. Ye, Relationship between the Size of the Samples and the Interpretation of the Mercury Intrusion Results of an Artificial Sandstone 11 (2018) 201.
[64] R. Pleau, P. Plante, R. Gagne, M.j.c., Pigeon, concrete, aggregates, Practical considerations pertaining to the microscopical determination of air void characteristics of hardened concrete (ASTM C 457 Standard) 12 (1990) 3–11.
[65] E. Schlangen, E.J.I.j.o.e.s. Garboczi, New method for simulating fracture using an elastically uniform random geometry lattice 34 (1996) 1131–1144.
[66] E. Schlangen, J.J.C. Van Mier, c. composites, Experimental and numerical analysis of micromechanisms of fracture of cement-based composites 14 (1992) 105–118.
[67] H. Zhang, Y. Xu, Y. Gan, Z. Chang, E. Schlangen, B.J.C. Šavija, C. Research Combined experimental and numerical study of uniaxial compression failure of hardened cement paste at micrometre length scale 126 (2019), 105925.
[68] M. Yip, J. Mohle, J.J.C.A.C. Bolander, I. Engineering, Automated modeling of three-dimensional structural components using irregular lattices 20 (2005) 393–407.
[69] Z. Qian, Multiscale modeling of fracture processes in cementitious materials, (2012).
[70] E. Schlangen, Z.J.J.o.M.M., Qian, 3D modeling of fracture in cement-based materials 1 (2009) 245–261.
[71] E. Schlangen, Experimental and numerical analysis of fracture processes in concrete, (1995).
[72] G. Lilliu, 3D analysis of fracture processes in concrete, Eburon Uitgeverij BV, 2007.
[73] H. Zhang, B. Šavija, S.C. Figueiredo, E.J.C. Schlangen, C. Research, Experimentally validated multi-scale modelling scheme of deformation and fracture of cement paste 102 (2017) 175–186.
[74] H. Zhang, B. Šavija, S. Chaves Figueiredo, M. Lukovic, E.J.M. Schlangen, Microscale testing and modelling of cement paste as basis for multi-scale modelling 9 (2016) 907.
[75] H. Zhang, B. Šavija, E.J.E.F.M. Schlangen, Combined experimental and numerical study on micro-cube indentation splitting test of cement paste 199 (2018) 773–786.
[76] H. Zhang, Y. Xu, Y. Gan, E. Schlangen, B.J.C. Šavija, C. Composites, Experimentally validated meso-scale fracture modelling of mortar using output from micromechanical models 110 (2020), 103567.
[77] A.M.J.P.o.C. Neville,, Properties of Concrete 36 (1996) 838–844.
[78] N. Arıoglu, Z.C. Girgin, E.J.A.M.J. Arıoglu, Evaluation of ratio between splitting tensile strength and compressive strength for concretes up to 120 MPa and its application in strength criterion 103 (2006) 18–24.
[79] G. Lavanya, J. Jegan, Evaluation of relationship between split tensile strength and compressive strength for geopolymer concrete of varying grades and molarity 10 (2015) 35523–35527.
[80] R. Kozul, D. Darwin, Effects of aggregate type, size, and content on concrete strength and fracture energy, University of Kansas Center for Research Inc, 1997 in,.
[81] E.P. Kearsley, P.J. Wainwright, The effect of porosity on the strength of foamed concrete, Cement and Concrete Research 32 (2002) 233–239.
[82] F. Pospisil, J. Jambor, J.J.A.i.A.A.C.A.B. Belko, Unit weight reduction of fly ash aerated concrete, (1992) 43-52.
[83] J. Suchorzewski, M. Nitka, Size effect at aggregate level in microCT scans and DEM simulation – Splitting tensile test of concrete, Engineering Fracture Mechanics 264 (2022), 108357.
[84] B.R. Indriyantho, Nuroji, Finite Element Modeling of Concrete Fracture in Tension with the Brazilian Splitting Test on the Case of Plane-stress and Plane-strain, Procedia Engineering 95 (2014) 252–259.
[85] M. Mazloom, H. Salehi, The relationship between fracture toughness and compressive strength of self-compacting lightweight concrete, in: IOP Conference Series: Materials Science and Engineering, IOP Publishing, 2018, p. 062007.
[86] A.S.f.T.a. Materials,, Standard Test Method for Linear-elastic Plane-strain Fracture Toughness K [Ic] of Metallic Materials, in, American Society for Testing and Materials, 2010.
[87] X. Hu, Q. Li, Z. Wu, S.J.E.F.M. Yang, Modelling fracture process zone width and length for quasi-brittle fracture of rock, concrete and ceramics 259 (2022), 108158.
[88] Y. Chen, X. Han, X. Hu, B. Wang, W.J.P.o.F.-X. Zhu, France, Strength criterion for size effect on quasi-brittle fracture with and without notch, (2019).
[89] X. Han, Y. Chen, X. Hu, W. Liu, Q. Li, S.J.E.F.M. Chen, Granite strength and toughness from small notched three-point-bend specimens of geometry dissimilarity 216 (2019), 106482.
[90] Y. Lu, X. Hu, X. Yang, Y. Xiao, Comprehensive tests and quasi-brittle fracture modeling of light-weight foam concrete with expanded clay aggregates, Cement and Concrete Composites 115 (2021), 103822.
[91] Z. Wu, S. Yang, X. Hu, J.J.E.F.M. Zheng, An analytical model to predict the effective fracture toughness of concrete for three-point bending notched beams 73 (2006) 2166–2191.
[92] J. Guan, X. Hu, X. Yao, Q. Wang, Q. Li, Z.J.M. Wu, Design,, Fracture of 0.1 and 2 m long mortar beams under three-point-bending 133 (2017) 363–375.
[93] D. Falliano, D. De Domenico, A. Sciarrone, G. Ricciardi, L. Restuccia, J. Tulliani, E. J.T. Gugliandolo, A.F. Mechanics, Fracture behavior of lightweight foamed concrete: the crucial role of curing conditions 103 (2019), 102297.
[94] W. Duckworth, Discussion of ryshkewitch paper by winston duckworth 36 (1953) 68.
[95] D.J.J.o.t.A.C.S. Hasselman,, Relation between effects of porosity on strength and on Young's modulus of elasticity of polycrystalline materials 46 (1963) 564–565.
[96] M.Y. Balshin, Relation of mechanical properties of powder metals and their porosity and the ultimate properties of porous metal-ceramic materials, Dokl Akad Nauk SSSR, in, 1949, pp. 831–834.
[97] K.J.C. Schiller, C. Research, Strength of porous materials 1 (1971) 419–422.
[98] G.J.J.o.t.I. McAdam, S. institute, Some relations of powder characteristics to the elastic modulus and shrinkage of sintered ferrous compacts 168 (1951) 346–358.
[99] R.M. Springgs, Expression for effect of porosity on elastic modulus of polycrystalline refractory materials, particularly aluminum oxide 44 (1961) 628–629.